Supplementary Materials for

Root and suppression of shuttling gain a uniform Li_2O interphase toward 610 Wh kg^{-1} lithium–sulfur batteries

Yu Wang *et al.*

Corresponding authors: Bing Han, bhan@eitech.edu.cn; Baojuan Xi, baojuanxi@sdu.edu.cn; Shenglin Xiong, chexsl@sdu.edu.cn

The PDF file includes:

Materials and Methods

Supplementary Text

Figs. S1 to S41

Tables S1 to S3

References

Materials and Methods

Chemicals

Electrolyte for lithium–sulfur batteries, 1M $LiN(CF_3SO_2)_2$ (LiTFSI) in DME: DOL=1:1 Vol% with 2% $LiNO_3$, was purchased from DoDoChem. Ethylene glycol dimethyl ether (DME, 99.5%), 1,3–Dioxolane (DOL, 99.5%), lithium fluoride (LiF, 99%), lithium sulfide (Li_2S, 99.9%), Vanadium pentoxide (V_2O_5, 99%), Manganese nitrate ($Mn(NO_3)_2\cdot 4H_2O$, 99.5%), Ferric nitrate ($Fe(NO_3)_3$, 99.9%), Cobaltous nitrate ($Co(NO_3)_2\cdot 6H_2O$, 99.5%), Nickel nitrate ($Ni(NO_3)_2\cdot 6H_2O$, 99.5%), Cupric nitrate ($Cu(NO_3)_2$, 99.5%), Zinc nitrate ($Zn(NO_3)_2\cdot 6H_2O$, 99.5%), ferrous sulfate ($FeSO_4\cdot 7H_2O$, 99%), thioacetamide (CH_3CSNH_2, 99%), manganese sulfate ($MnSO_4\cdot H_2O$, 99%), zinc sulfate ($ZnSO_4\cdot 7H_2O$, 99.9%), and sodium sulfide ($Na_2S\cdot 9H_2O$, 99.5%) were purchased from Aladdin Chemical Co., Ltd. Sublimed sulfur powder (S_8, 99.999%), hydrochloric acid (HCl, 36%~38%), glacial acetic acid (C_2H_5COOH, 99.5%), sodium hydroxide (NaOH, 99.9%), ethylene glycol ($HOCH_2CH_2OH$, 99.9%), copper sulfate ($CuSO_4\cdot 5H_2O$, 99.9%) were purchased from Sinopharm Chemical Reagent Co., Ltd. Tetrabutyl titanate ($C_{16}H_{36}O_4Ti$, 99%) and ammonium metavanadate (NH_4VO_3, 99.9%) were purchased from Shanghai Macklin Biochemical Co., Ltd. Titanium aluminum carbide powder (Ti_3AlC_2, 99%) was purchased from Laizhou Kai Kai Ceramic Materials Co., Ltd. Deionized water (18.0 MΩ cm^{-1}) used in all experiments was prepared by pan ultra–pure purification system.

Synthesis of Li_2S_6 solution

The synthesis of Li_2S_6 was carried out using the reaction between S_8 and Li_2S. To ensure accuracy, 0.4595 g of Li_2S and 1.603 g of sulfur, in a molar ratio of 8:5, were precisely weighed and placed in a volumetric flask. Subsequently, 9.5 mL of a DOL: DME = 1:1 mixed solution was added. The mixture was stirred for 48 hours to ensure the complete dissolution and reaction. Following this, the solution was diluted with the mixed solvent to a final volume of 10.00 mL, resulting in a precise 1.00 M Li_2S_6 solution. All procedures were conducted within a glovebox to maintain the control over the environment.

Determination of the Li_2S_6 working curve

In the UV–Vis absorption working curve test for Li_2S_6, pure DME was chosen as the solvent. This is because the DOL/DME (1:1 volume ratio) mixed solvent evaporates quickly, making it difficult to ensure accurate concentrations. A 1.00 M Li_2S_6 in DME solution was synthesized using the same method to the above procedure and then sequentially diluted to 0.4, 0.6, 0.8, and 1.0 mM. The solutions were transferred to screw–thread corvettes in a glove box, and UV–Vis absorption measurements were conducted. The absorbance at a wavelength of 350 nm was used for linear fitting to obtain the Li_2S_6 working curve.

Preparation of the sulfur cathode

First, sublimed sulfur powder and black carbon (BP2000) were mixed and ground at a mass ratio of 7:3. The mixture was then sealed and stored in an ampoule under an argon atmosphere. The ampoule was placed in a tube furnace and subjected to a specific thermal treatment program. It was first held at 155 °C for 12 hours, then heated to 220 °C and maintained for 4 hours. The obtained sulfur/carbon mixture, Ketjen Black (KB), carbon nanotubes (CNT), and polyvinylidene fluoride (PVDF) were mixed in a mass ratio of 7:1:1:1. A suitable amount of N–methyl–2–pyrrolidone (NMP) solvent was added, and the mixture was ball–milled for 3 hours to prepare the cathode slurry. The slurry was then coated onto carbon–coated aluminum foil using a 200 μm thick blade and dried in a vacuum oven at 60 °C. Finally, it was punched into 12 mm diameter discs, with a sulfur content of approximately 1.0 mg per square centimeter.

CV measurements and potential–current equation fitting for LSBs

For the assembly of LSBs, a 12 mm diameter sulfur cathode aforementioned and a 16 mm diameter lithium anode were used. The LSBs were assembled in CR2016 coin cells, with a commercial Celgard 2400 separator and 1 M LiTFSI in DOL/DME (1:1 volume ratio) with 2% $LiNO_3$ as the electrolyte in an argon–filled glove box (H_2O, $O_2<0.5$ ppm). The CV measurements were conducted within the potential range of 1.7–2.8 V vs. Li^+/Li at various scan rates (0.1–0.5 mV s^{-1}). The first derivative of the CV curves during the discharge process was obtained, and the Savitzky–Golay method with a second–order polynomial was used to smooth the first derivative curve followed by further differentiation. The voltage point corresponding to the minimum around 2.1–2.2 V indicates the point where the proportion of Li_2S_6 intermediate reaches nearly 100%. By taking the logarithm of the current and fitting the voltage (V) and log(i) of five points, the potential–current equation for the Li_2S_6 point can be obtained.

Solving the Li_2S_6 conservation equation

The batteries were discharged at different currents to the calculated P_{26} cutoff voltage and then, immediately placed in liquid nitrogen to prevent further shuttling, thereby avoiding errors from time–related factors. After transferring to an argon–filled glove box, they were disassembled and the Li_2S_6 on the cathode side was rinsed multiple times with DME, including the cathode sheet and the side of the separator adjacent to cathode. The obtained Li_2S_6 in DME solution was added into a 10.00 mL volumetric flask and diluted to the mark for the following UV–Vis absorption measurements.

Finite Element Analysis (FEA) simulations

The FEA simulations are performed with the COMSOL Multiphysics software. The FEA models shown below were defined by the law of mass conservation and electroneutrality assumption of related ions without considering possible side reactions. Simulations consider the influence of two different factors on ion concentration: concentration diffusion and electric field migration. Therefore, three different simulation models were constructed to verify the effects of these two factors: 1) The diffusion coefficient of the model is set very low, and there is no potential difference inside the electrolyte. In this case, the concentration of Li_2S_6 produced is the total cumulative concentration during the charging process; 2) The diffusion coefficient of the model is set to the conventional ion diffusion coefficient, and there is no potential difference inside the electrolyte. In this case, the concentration distribution of Li_2S_6 inside the electrolyte is caused by concentration diffusion; 3) The diffusion coefficient of the model is set to the conventional ion diffusion coefficient, and there is a potential difference inside the electrolyte. In this case, the concentration distribution of Li_2S_6 inside the electrolyte is caused by the superposition of concentration diffusion and electric field migration.

Under the combined action of electric field migration and concentration diffusion, the anions and cations move in different directions, eventually reaching a steady state. Using the current distribution and concentration diffusion equation to track the current and concentration distribution, the flux of each ion in the electrolyte can be calculated by Nernst-Planck equation, $N_\mathrm{i} = -D_i\left(\nabla c_i + \frac{F}{RT} z_i c_i \nabla \Phi_l\right), i = 1, 2, \ldots, n$, where $D_i, N_i, c_i, z_i, F, T, R,$ and Φ_l denote the diffusion coefficient, the flux, the concentration, the charge number, the Faradaic constant, temperature, gas constant, and electrolyte potential, respectively. L stands for the position along the diffusion region of thickness d (0 < L < d). Based on the steady-state continuity equations and the law of mass conservation, we have $\frac{\partial c_i}{\partial t} + \nabla N_i = 0$ and the electroneutrality assumption was represented as $F\sum_{i=1}^{n} z_i c_i = 0$. The boundary condition was set as $\vec{n} \cdot J = 0$. The simulation steps include a current distribution initialization and a steady step. The initial concentration is set to 0 mol m^{-3}. The potential difference within the electrolyte is set to 0.5 V–0.1 V. In the simulations, it is considered that 19% of Li_2S_6 is ionized and can be driven by the electric field, so the force of electromigration is set to 19% of its original magnitude. From now on, all physical fields and boundary conditions have been described clearly.

H–shaped visualization cell assembly

A sealed 20–20 mL two–electrode electrolysis cell was used as the cell compartments. The dimensions of the sulfur cathode and lithium foil as anode were 2 cm × 5 cm, which were connected to external wires via platinum clips. The cell compartments were separated using a Celgard 2400 membrane to isolate the cathode from the anode. The electrolyte used was 1 M LiTFSI in DOL/DME (1:1 volume ratio) with 2% $LiNO_3$. The current applied during the test was 2.0 mA.

Synthesis of various transition metal compounds (TMCs)

Synthesis of TiO_2: Add 50 mL of ethanol to a beaker and slowly introduce 10 mL of tetrabutyl titanate. Under stirring, gradually add 20 mL of deionized water to form a white precipitate, followed by stirring for 6 hours, and then filter to collect the precipitate. Wash the product several times with deionized water and ethanol, then transfer it to a drying oven set at 60 °C for 24 hours to obtain the dry powder. Finally, place the dried powder in a tube furnace and calcine at 500 °C for 4 hours to remove organic impurities and enhance the crystallinity of TiO_2.

Synthesis of VO_2: Dissolve 0.73 g of V_2O_5 in 30 mL of deionized water and stir for 10 minutes. Add 0.5 mL of glacial acetic acid and continue stirring for 30 minutes. Transfer the mixture to a 50 mL autoclave and maintain at 180 °C for 24 hours. After cooling, wash the product five times with water. Then, place the washed product in a drying oven at 60 °C for 24 hours to obtain VO_2 powder.

Synthesis of MnO, Fe_2O_3, Co_3O_4, NiO, CuO and ZnO: The synthesis of these six oxides follows the precipitation-calcination method. Dissolve 1.5 g of the corresponding metal nitrate in 100 mL of water and stir thoroughly until completely dissolving. Add 0.5 g of NaOH powder and stir for 1 hour to ensure uniform reaction. Perform vacuum filtration and wash the resulting product. Finally, calcine the product in air at 600 °C for 3 hours to obtain the corresponding oxides.

Synthesis of TiN and VN: Place an appropriate amount of the above-obtained TiO_2 or VO_2 in a tube furnace and calcine at 600 °C for 5 hours under an ammonia atmosphere to obtain the corresponding nitrides.

Synthesis of VS_2 and FeS_2: Add 0.5 g of ammonium metavanadate or ferrous sulfate and 1.5 g of thioacetamide to 30 mL of ethylene glycol and stir uniformly under ambient temperature using magnetic stirring. Transfer the precursor solution into a PTFE-lined autoclave and react at 160 °C for 12 hours under sealed conditions. After the reaction is complete, allow the mixture to cool naturally to room temperature. Wash the product alternately with water and ethanol three times. Then, dry the washed product in a 60 °C oven for 24 hours to obtain dry VS_2 or FeS_2 powder.

Synthesis of MnS, CuS and ZnS: These three sulfides were synthesized using a double displacement reaction. Dissolve 3.5 g of $MnSO_4$, $CuSO_4$, or $ZnSO_4$ (including crystallization water) in 50 mL of deionized water and stir until completely dissolving. Dissolve 3.8 g of $Na_2S\cdot 9H_2O$ in 50 mL of deionized water to prepare a solution. Gradually add the sodium sulfide solution dropwise to the above sulfate solution under stirring. After reacting for 2 hours, perform vacuum filtration to collect the product, and wash multiple times with water to remove any residual soluble salts. Finally, dry the washed product in a 60 °C oven for 24 hours to obtain dry MnS, CuS, and ZnS powder.

Synthesis of $Ti_3C_2T_x$: First, 1.0 g of Ti_3AlC_2 MAX phase powder was slowly added to a mixture of 20 mL of 9 M hydrochloric acid (HCl) and 1.2 g of lithium fluoride (LiF) under constant stirring. The reaction mixture was then stirred at 35 °C for 24 hours to selectively etch out the aluminum layer. After the etching process, the resulting suspension was washed with deionized water several times until the pH reached approximately 6–7. Then, after centrifugation at 2000 rpm for 2 minutes, the few–layer $Ti_3C_2T_x$ in the supernatant was collected and freeze–dried to obtain solid $Ti_3C_2T_x$.

Preparation of the TMC cathode

Each used TMC and PVDF in a 9:1 mass ratio was introduced into an appropriate quantity of NMP and ground for 30 minutes to achieve a homogeneous slurry. By employing a 200 μm thick blade, the slurry was evenly spread onto carbon–coated aluminum foil. After drying in an oven at 60 °C for 3 hours and then in a vacuum oven for further dehydration and deoxidation, it was punched into 12 mm diameter discs to obtain TMC cathode for subsequent use.

Preparation of the TMC@PP

Each solid TMC and PVDF in a 9:1 mass ratio was introduced into an appropriate quantity of NMP and ground for 30 minutes to achieve a homogeneous slurry. Using a 100 μm thick blade, the slurry was evenly spread over commercial PP membrane (Celgard 2400). After drying it in an oven at 60 °C for 3 hours and then in a vacuum oven for further dehydration and deoxidation, it was punched into 19 mm diameter discs to obtain TMC@PP functional separators.

Preparation of pre–lithiated separator (Li_xTMCs@PP)

Using aluminum foil with a diameter of 19 mm as the current collector, the corresponding TMC@PP served as both the separator and the cathode for the Li||TMC battery assembly. The initial potential of the battery was approximately 3.0 V, and it was discharged at a constant current to 2.1 V to render the formation of the in–situ lithiated separator. Subsequently, the battery was disassembled in a glove box, and the separator was rinsed with a DOL/DME (1:1 volume ratio) mixture, resulting in Li_xTMCs@PP.

In situ impedance testing

The assembled LSBs with PP and $Ti_3C_2T_x$@PP were respectively discharged at a constant current of 0.1 mA. Impedance tests were conducted sequentially at cut–off voltages of 2.80, 2.50, 2.35, 2.30, 2.20, 2.15, 2.05, 1.90, and 1.70 V. The frequency range for the tests was set from 0.1 Hz to 10^5 Hz.

Assembly and testing of symmetrical cells

A symmetric battery was assembled using aluminum foil as the current collector and Li_2S_6 in DME:DOL= 1:1 Vol% with 2% $LiNO_3$ as the electrolyte. The CR2016 coin cells were assembled in a glove box, utilizing $Li_yTi_3C_2T_x$@PP, $Ti_3C_2T_x$@PP, and PP as separators, with 30 μL of the

Li_2S_6 electrolyte added. The voltage range for the CV test was set from –0.8 to 0.8 V at a sweep speed of 0.2 mV s^{-1}.

Electrochemical deposition and cryogenic specimen preparation

Sulfur served as one electrode, with lithium metal functioning as another electrode with a copper grid for transmission electron microscope (TEM) placed on the lithium metal. The sulfur active material in the cell is 0.8 mg, and the cycling current is 0.2 C. Batteries were disassembled in an argon-filled glovebox (O_2 < 0.01 ppm, H_2O < 0.01 ppm) and the deposited grid was rinsed briefly with pure DME to remove residual lithium salts, followed by freezing. Then, the deposited grids were rapidly plunge-frozen in liquid nitrogen to vitrify specimens at their native room-temperature structure. All subsequent handling, including storage, transport, autoloader loading was performed under continuous liquid nitrogen protection to prevent environmental degradation of specimens. The cycled sulfur cathode was rinsed with pure DME and then scraped onto the TEM copper grid.

Ultra-low-dose cryo-electron microscopy imaging technology

Ultra-low-dose cryo-electron microscopy imaging technology employs rapid vitrification at cooling rates of 10^4-10^6 K s^{-1} to immobilize the specimen’s native room-temperature structure, preserving its intrinsic conformational states. Subsequent imaging is performed using cryo-high-resolution transmission electron microscopy (cryo-HRTEM) under liquid-nitrogen temperature conditions, which suppresses molecular thermal motion and enhances radiation tolerance in beam-sensitive materials. By integrating precise specimen localization, dose fractionation, high-efficiency direct electron detection, and motion-correction algorithms, the cumulative electron dose is substantially reduced while maintaining high signal-to-noise ratios. Finally, advanced iterative filtering and reconstruction algorithms are applied to the low-dose images to generate an atomic-resolution structural model.

Electrochemical deposition and cryogenic specimen preparation

Sulfur served as one electrode, with lithium metal functioning as another electrode with a copper grid for cryogenic transmission electron microscope (Cryo-TEM) placed on the lithium metal. The sulfur active material in the cell is 0.8 mg, and the cycling current is 0.2 C. After one cycle, batteries were disassembled in an argon-filled glovebox (O_2 < 0.01 ppm, H_2O < 0.01 ppm) and Cu grid deposited with lithium metal from the sulfur cathode was rinsed briefly with pure DME to remove residual lithium salts. For cryogenic vitrification using a Vitrobot system, the foam chamber and cup were pre-cooled with liquid nitrogen until boiling ceased, followed by introduction of liquid ethane. The grid was secured with specialized tweezers, rapidly plunged into the liquid ethane bath to vitrify the specimen, and thus preserve its native room-temperature structure. After vitrification, the grid was transferred under cold nitrogen vapor into a pre-cooled storage box and gently detached from solidified ethane. The grid box was stored in a liquid nitrogen dewar. All subsequent handling, including storage, transport, autoloader loading was performed under continuous liquid nitrogen protection to prevent environmental degradation of specimens. For sulfur specimens, the cycled cathode was rinsed with pure DME and scraped directly onto a TEM copper grid, followed by identical vitrification and transfer protocols as applied to the lithium samples.

Cryogenic transmission electron microscope characterization

High-resolution TEM image was performed using ultra-low-dose cryo-electron microscopy imaging technology. All cryo-TEM characterization were conducted using an aberration-corrected FEI Krios G3i microscope (D3845) operating at 300 kV, equipped with a Falcon 3 direct electron detector (Falcon 3EC, information limit: ~0.14 nm). An automated liquid nitrogen filling system maintained the sample chamber and lens barrel at approximately -192 °C for extended periods (several days) to ensure thermal stability during high-resolution imaging. Specimens were initially navigated and focused at a low magnification of 5.0 kx under an ultra-low electron dose (<0.01 e $Å^{-2}$ s^{-1}). High-resolution images were subsequently acquired at 152.9 kx under strict dose-control conditions (8-10 e $Å^{-2}$ s^{-1} for 10 s). To mitigate beam-induced damage and correct for sample drift, the total exposure was partitioned into 66 consecutive sub-frames. These sub-frames were aligned and integrated using a real-time motion-correction algorithm, which computationally compensated for specimen displacement, restored high-frequency information otherwise lost to motion, and substantially reduced the cumulative electron dose.

Atomic-Resolution Image Filtering for Cryo-TEM

Atomic-resolution cryo-TEM images were processed using DigitalMicrograph (Gatan Inc.). First, image processing was performed in DigitalMicrograph (Gatan Inc.). Cryo-TEM micrographs were first transformed into frequency-domain representations via fast Fourier transform (FFT).

Diffraction spots in reciprocal space were systematically identified and labeled. Circular masks were calibrated to isolate target diffraction regions for selective frequency extraction. A low-pass filter was applied using the Mask function to retain lattice-periodic signals while suppressing high-frequency noise. Finally, inverse FFT was executed on the filtered frequency-domain data to reconstruct noise-reduced atomic-resolution images, clearly revealing ordered atomic columns and lattice defects. This workflow proved essential for resolving beam-sensitive structural features under low-dose conditions.

Test of shuttle current

To measure the shuttle current, 1M LiTFSI in DOL/DME=1:1 was employed to avoid passivation of the lithium anode. Initially, the lithium–sulfur cells underwent three charge–discharge cycles, followed by a galvanostatic charge to 2.8 V at a current density of 0.2 C. Subsequently, the cells were discharged to 2.38 V and transitioned to a potentiostatic mode, during which the shuttle current peaked. After a period of stabilization, the steady-state potentiostatic current was recorded as the shuttle current.

The assembly of pouch batteries

The preparation of slurry for sulfur cathode is similar to the part in Preparation of the sulfur cathode except the mass ratio of sulfur/carbon mixture, carbon nanotubes (CNT), and PVDF was 8:1:1 to increase the sulfur content. The slurry was then coated onto carbon–coated aluminum foil using a 1000 μm thick blade and dried in a vacuum oven at 60 °C. Finally, it was punched into 5.6×8.6 cm sheets, with a sulfur content of approximately 7.5 mg per square centimeter. The lithium strip has dimensions of 5.9 cm × 8.8 cm × 200 μm. The separator is $Ti_3C_2T_x$@PP, measuring 6 × 9 cm. During assembly, two single–sided positive electrodes and six double–sided positive electrodes were used to get the active sulfur mass totaling 6.35 g.

Physicochemical characterizations

Structure of products was discovered by powder X–ray diffractometer (XRD, Bruker D8 Advance, Cu Kα, and λ=1.5418 Å). The transmission electron microscopy (TEM) measurements (TALOS F200X with accelerating voltage of 200 kV) and high–angle annular dark–field scanning transmission electron microscopy (JEOL JEM–ARM200F) were used to check sizes, morphology and structures of samples. The X–ray photoelectron spectra (XPS) were gathered on an X–ray photoelectron spectrometer (Thermo ESCALAB 250 Xi) with Al Kα (hν = 1486.6 eV) as X–ray source. To evaluate porous structure, nitrogen adsorption–desorption isotherms at 77 K were recorded using Autosorb 6B apparatus. AMETEK Princeton Applied Research VersaSTAT 3F instrument was employed for electrochemical tests. UV–Vis absorption spectra were measured using a Puxi T600B UV–Vis spectrophotometer. Aberration-corrected imaging was performed using an FEI Krios G3i microscope (Serial No. D3845) operating at 300 kV, equipped with a Falcon 3 direct electron detector (information limit: ~0.14 nm). An automated liquid nitrogen replenishment system maintained the sample chamber and lens column at approximately -192 °C for multiple days to ensure thermal stability during high-resolution imaging. Electron paramagnetic resonance measurements were performed on a CIQTEK EPR200 spectrometer using 1D field-sweep mode. The ^{7}Li nuclear magnetic resonance (NMR) spectrum was obtained using a 400 MHz AVANCE III HD400 NMR spectrometer with a MAGNET SYSTEM 400/54 ASCEND magnet, a magnetic field strength of 9.397 Tesla, and a 54 mm room temperature chamber.

Supplementary Text

Derivation of activation energy from Tafel slope

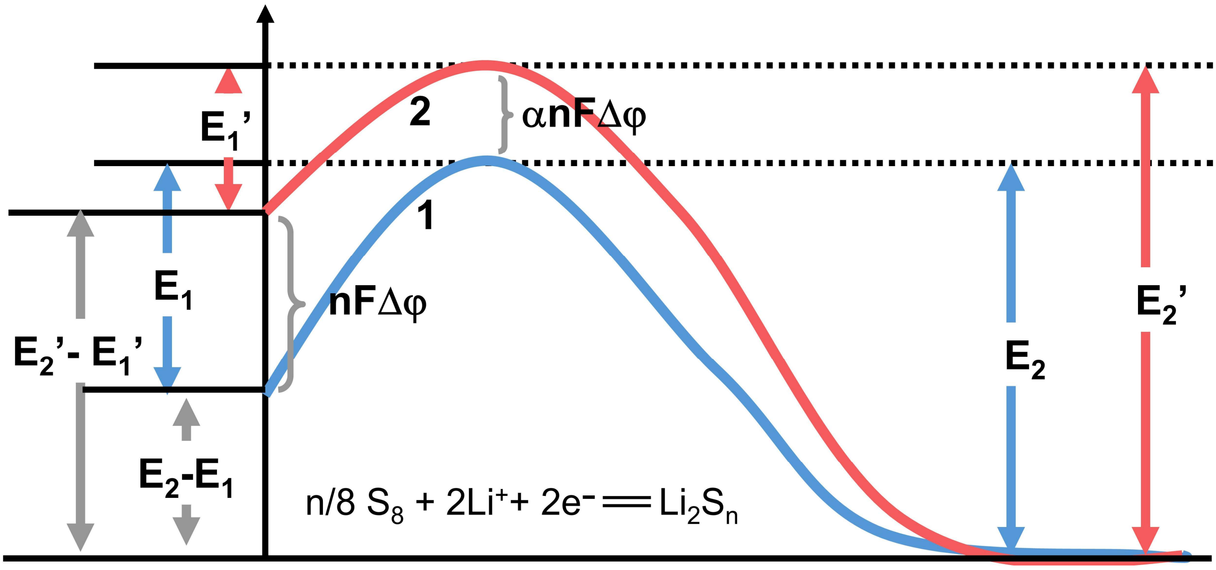

Note: For the SRR reaction n/8 S_8 + $2Li^+$ + $2e^-$ $=$ Li_2S_n, the electrons at the electrode can be considered as reactants. As the potential decreases, the energy of electrons changes, thereby raising the initial energy by $nF\Delta\varphi$, which consequently affects the activation energy.

From the figure, the relationship can be derived as follows:

$$E_2' - E_1' = E_2 - E_1 + nF\Delta\varphi$$

Transposition: $(E_2' - E_1') - (E_2 - E_1) = nF\Delta\varphi$

Let: $E_2' - E_2 = \alpha nF\Delta\varphi, E_1' - E_1 = -\beta nF\Delta\varphi, \alpha + \beta = 1$

Thus: $E_2' = \alpha nF\Delta\varphi + E_2, E_1' = -\beta nF\Delta\varphi + E_1$

According to the kinetic equation: $v = kc^x$

Arrhenius equation: $k = Ae^{-\frac{E_a}{RT}}$

Faraday's equation: $i_c = nFv$

Consequently, we obtain: $i_c = nFAc^x e^{-\frac{E_a}{RT}}$

Given the initial potential as φ^0, the electrode process kinetics equation is as follows for a potential φ:

$$i_c = nFAc^x e^{-\frac{E_1^0 - \beta nF(\varphi^0 - \varphi)}{RT}} = nFAc^x e^{-\frac{E_1^0 - \beta nF\varphi^0}{RT}} \times e^{-\frac{\beta nF\varphi}{RT}} = i_c^0 e^{-\frac{\beta nF\varphi}{RT}}$$

Taking the logarithm, we obtain:

$$\log i_c = \log i_c^0 - \frac{\beta nF}{2.3RT}\varphi$$

Rearrangement: $\varphi = \frac{2.3RT}{\beta nF}\log i_c^0 - \frac{2.3R}{\beta nF}\log i_c$

Thus, the difference in activation energy is:

$$E_a = E_a^0 + \alpha nF\Delta\varphi - nF\Delta\varphi = E_a^0 - \beta nF\Delta\varphi$$

Utilizing the Tafel slope: $k = \frac{2.3RT}{\beta nF}$

Thus: $E_a = E_a^0 + \frac{2.3R}{k}\Delta\varphi = E_a^0 + \frac{2.3R}{k}(\varphi^0 - \varphi)$

$$\Delta E_a = 2.3RT(\varphi^0 - \varphi)(\frac{1}{k_2} - \frac{1}{k_1})$$

Note: φ^0 is taken as the initial potential of 2.8 V.

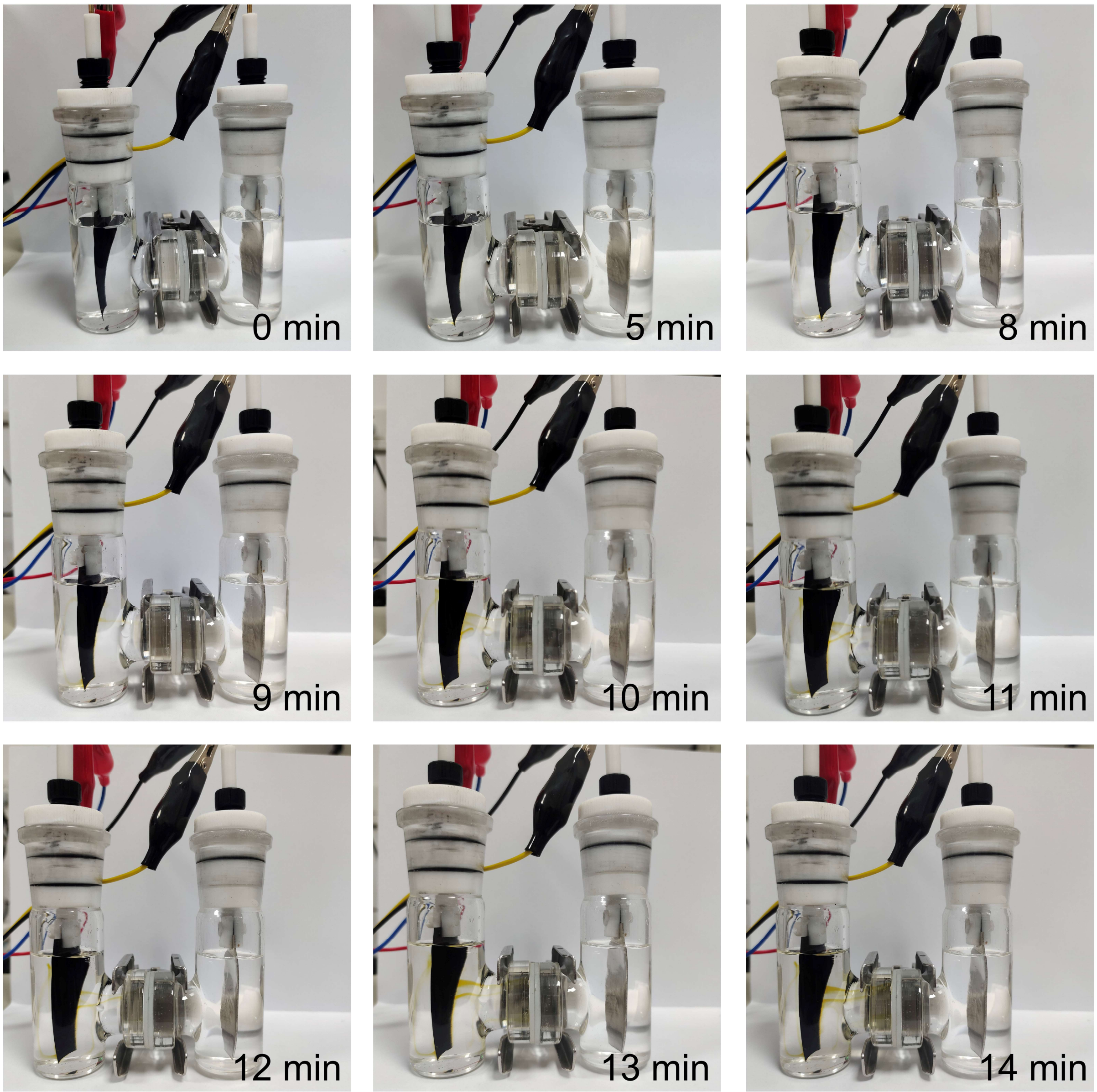

Supplementary Fig. 1 | Digital photographs of the discharge process in the H-type lithium–sulfur cell. The sulfur cathode is positioned on the left along with the lithium anode on the right. The polysulfides exhibit a characteristic yellow hue, allowing their formation and migration in the electrolyte to be directly visualized. Because the electrode spacing in an H-type cell is far greater than in conventional coin or pouch cells, the system experiences more pronounced concentration polarization—yet this “magnification effect” enables the diffusion behavior of polysulfides to be captured with remarkable clarity. At the beginning of discharge, no visible color change appears because the first product Li_2S_8 has a very low solubility (only ~0.01 mol L^{-1}). After 5 minutes, a pale-yellow region emerges at the electrode edges, indicating locally enhanced reaction activity. By 8–9 minutes, rapid formation of Li_2S_6 deepens the yellow tint throughout the cell. After 10 minutes, the horizontal spread of the yellow species becomes strikingly apparent. If diffusion was driven solely by concentration gradients, the polysulfides would be expected to propagate at comparable rates horizontally and vertically, producing a semicircular front. Instead, the experiments reveal a pronounced preference for horizontal migration. This atypical diffusion pathway signifies that the motion of polysulfides is governed not only by concentration gradients but also by an additional driving force—one directed horizontally from the cathode toward the anode.

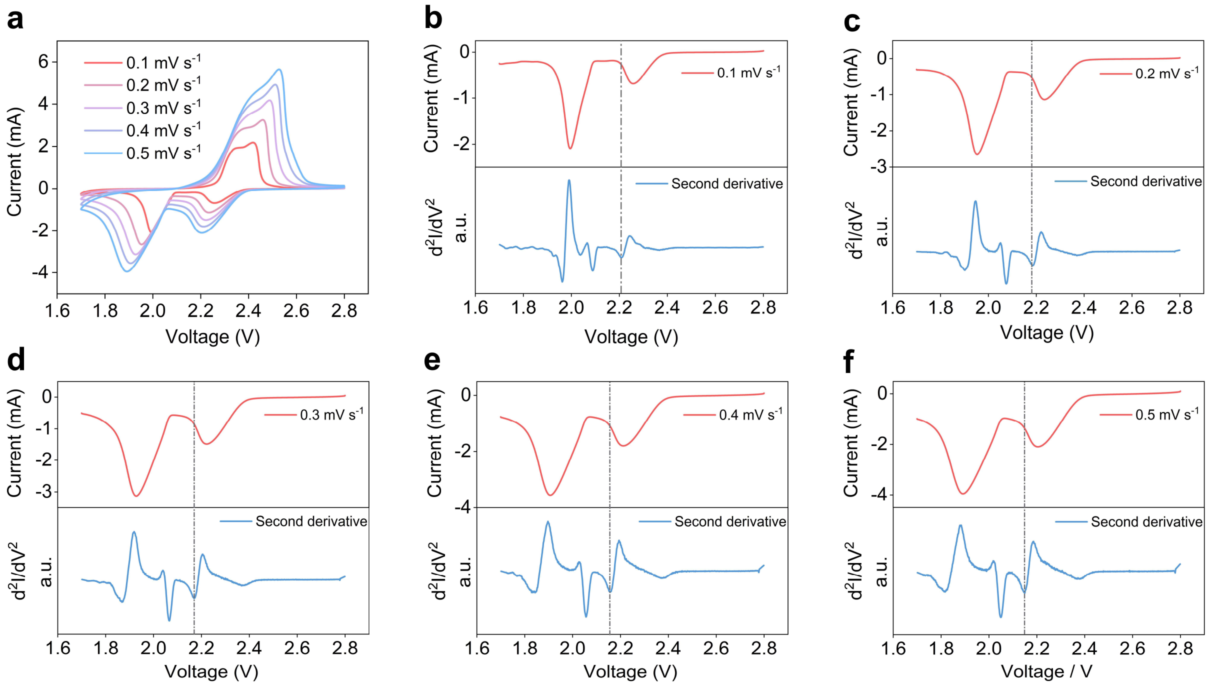

Supplementary Fig. 2 | Derivative-feature-enabled kinetic analysis of sulfur redox reactions in LSBs. a, CV curves of the LSBs at various scan rates. **b–f**, Discharge curves and their second derivatives from 0.1 to 0.5 mV s^{-1}. Theoretical analysis shows that the voltage and current corresponding to third-derivative zero points should lie on a linear V–logI relationship. However, experimental CV curves are not strictly analytic, and repeated differentiation amplifies noise, making direct identification of third-derivative zeros unreliable. To overcome this limitation, the extremum of the second derivative was used as a robust surrogate. The marked minima yield voltages and log I values that fall precisely on the linear trend, and two additional unmarked minima also conform to the same relationship. This derivative-feature-based approach is resistant to noise and particularly useful for lithium–sulfur systems, where multistep sulfur redox reactions produce overlapping peaks and complex interfacial behavior. The linear V–logI correlation enables extraction of key kinetic potentials without peak deconvolution, offering a clearer and more comparable kinetic interpretation of the sulfur redox network.

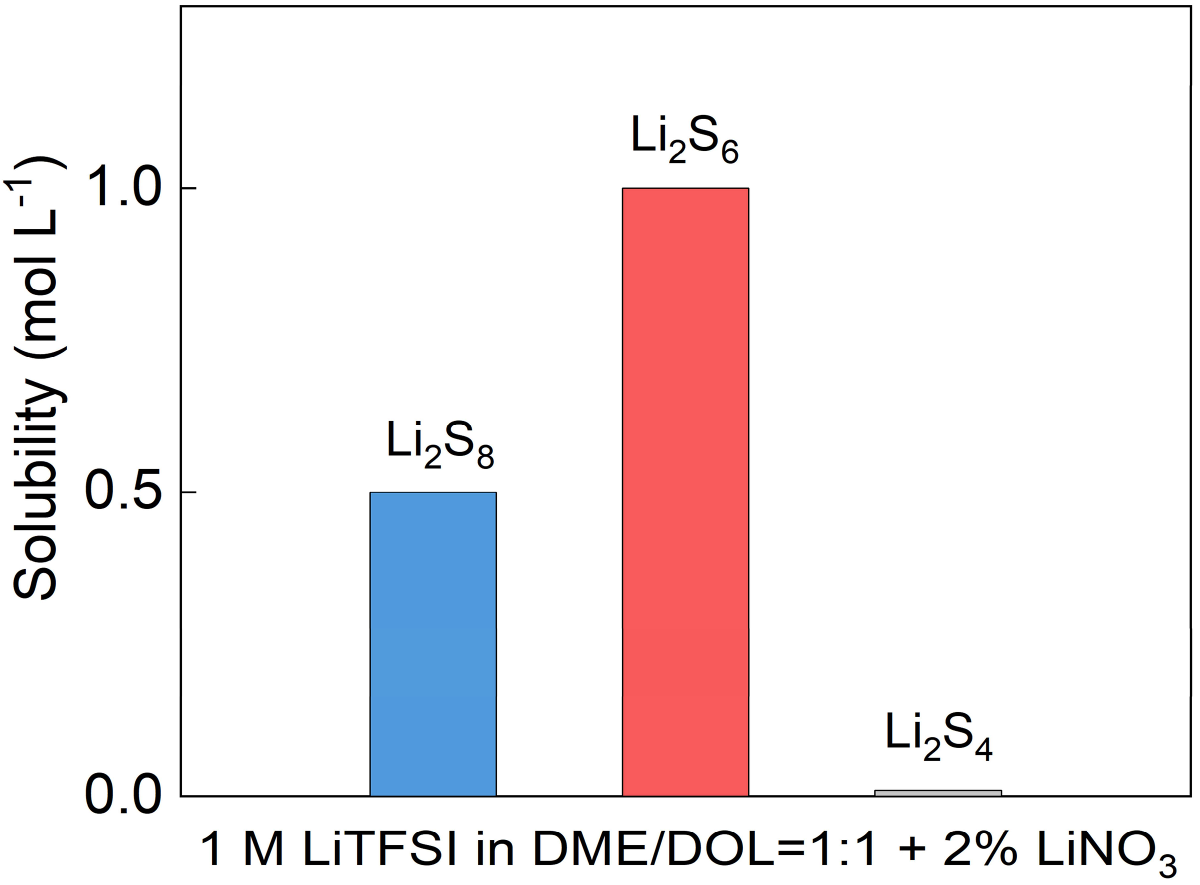

Supplementary Fig. 3 | The solubility of three typical polysulfides. The Li_2S_8, Li_2S_6, and Li_2S_4 in LSB electrolyte is approximately 0.5 M, 1.0 M, and 0.01 M respectively.

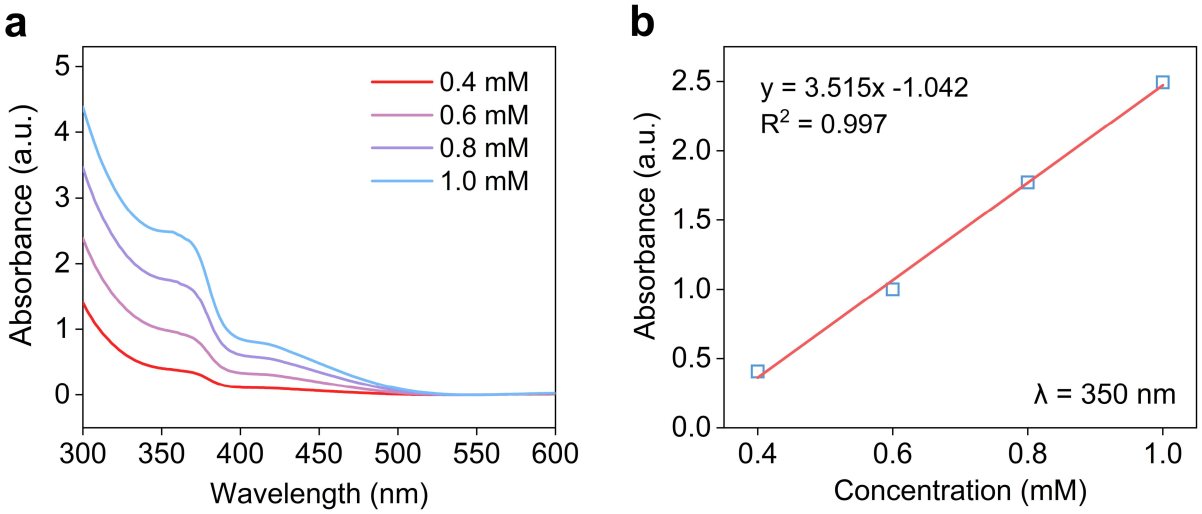

Supplementary Fig. 4 | UV–Vis absorption spectroscopy test for the concentration of Li_2S_6 solution at 350 nm. a, UV–Vis absorption curves of 0.4–1.0 mM Li_2S_6 in DME solvent. **b**, Standard curve for the concentration of Li_2S_6 ranging from 0.4 to 1.0 mM.

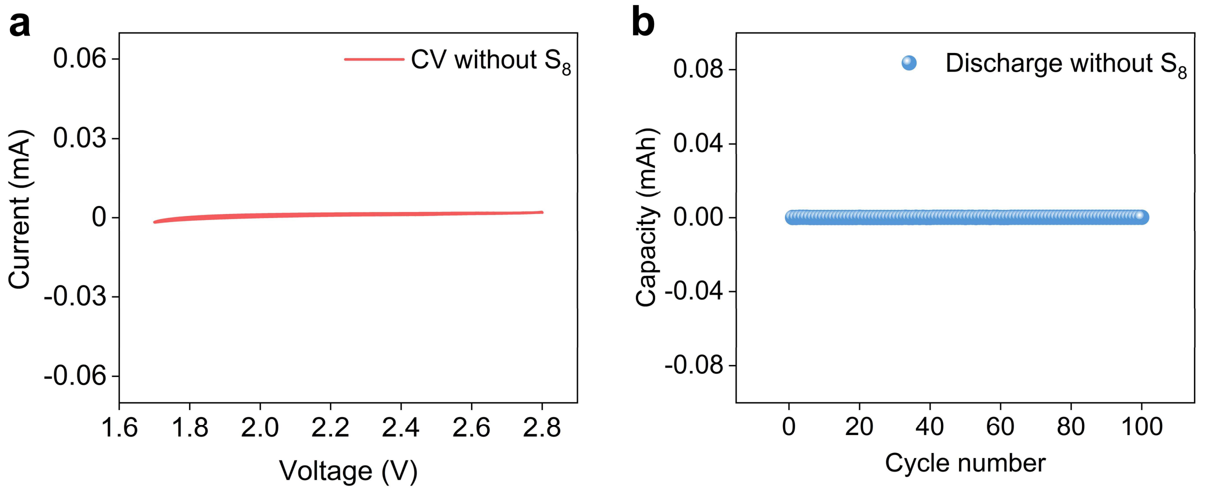

Supplementary Fig. 5 | The comparison curve without the active material sulfur. a, CV curve. **b**, cycling performance of a sulfur-free battery. This indicates that the discharge capacity is entirely contributed by the active material sulfur.

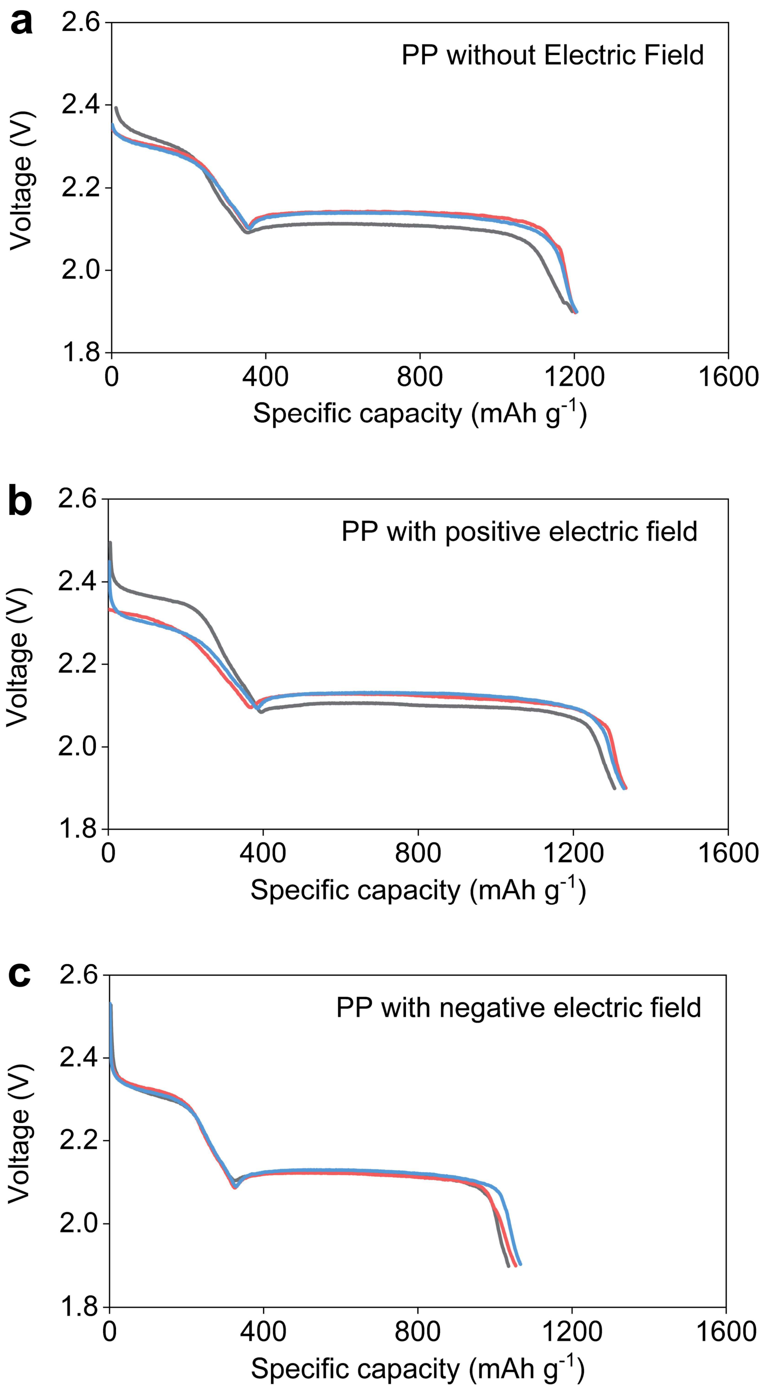

Supplementary Fig. 6 | Discharge curves of LSBs under three conditions: (**a**) without external field, (**b**) an external field aligned with the internal field during discharge, and (**c**) an external field opposite to the internal field. Applying a forward external field increases both the discharge capacity and the ratio of capacities for the second plateau to the first, whereas a reverse external field leads to a decline in both metrics.

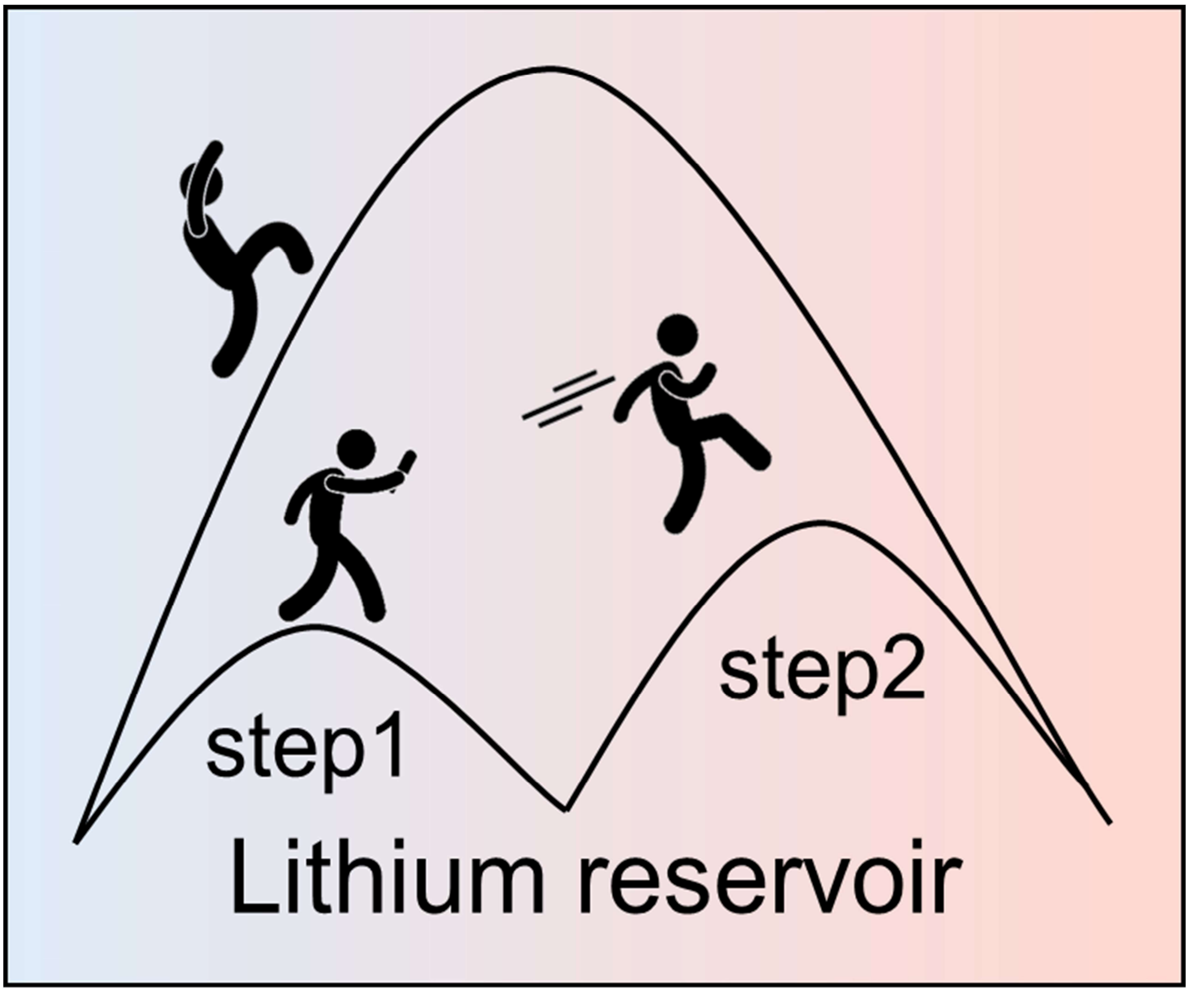

Supplementary Fig. 7 | Schematic illustration of the lithium reservoir strategy. Constructing a lithium-ion buffering zone on the separator between the cathode and anode transforms the conventional single-step diffusion process into a continuous low-energy-barrier diffusion within the lithium reservoir region.

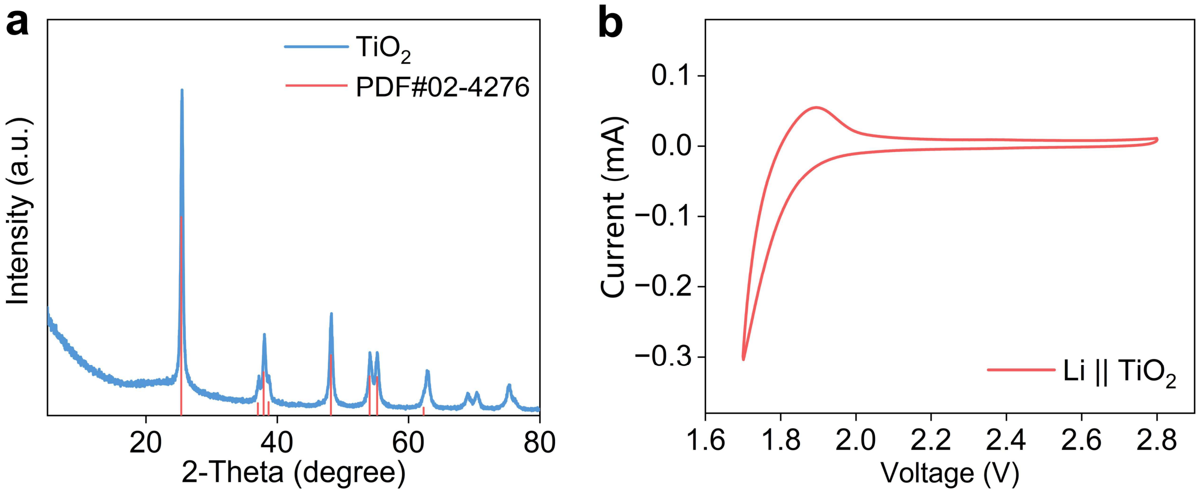

Supplementary Fig. 8 | The structural identification and electrochemical response of TiO_2. **a**, XRD pattern of TiO_2, showing good agreement with the standard diffraction peaks (PDF#02-4276) and confirming the crystalline phase of TiO_2. **b**, Cyclic voltammetry curve of TiO_2 versus Li/Li^+, recorded over the indicated voltage window, revealing the electrochemical response of the TiO_2 electrode in a lithium half-cell configuration.

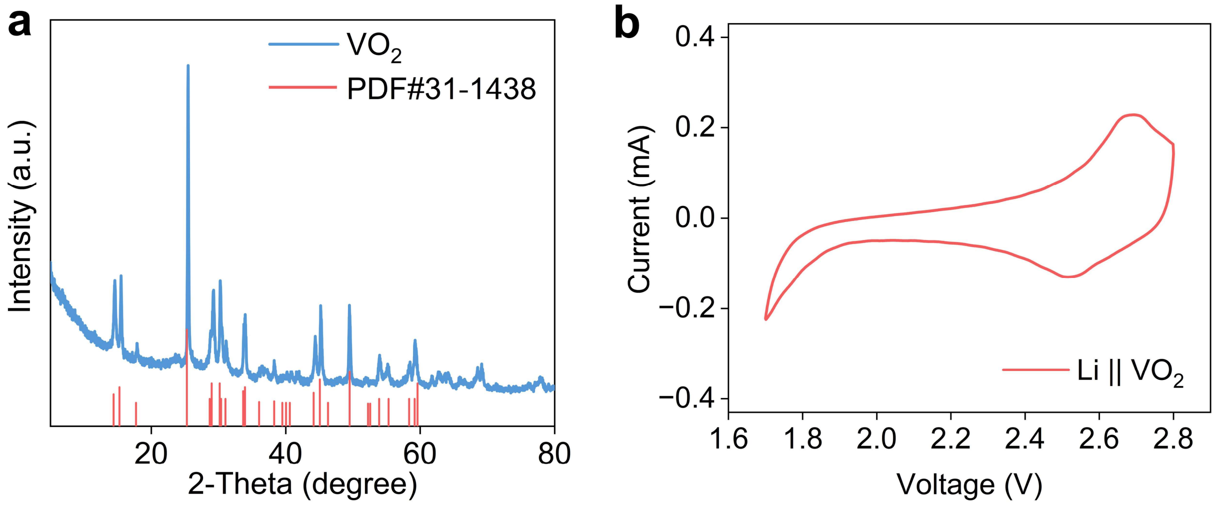

Supplementary Fig. 9 | The structural identification and electrochemical response of VO_2. **a**, XRD pattern of VO_2, showing good agreement with the standard diffraction peaks (PDF#31-1438) and confirming the crystalline phase of VO_2. **b**, Cyclic voltammetry curve of VO_2 versus Li/Li^+, recorded over the indicated voltage window, revealing the electrochemical response of the VO_2 electrode in a lithium half-cell configuration.

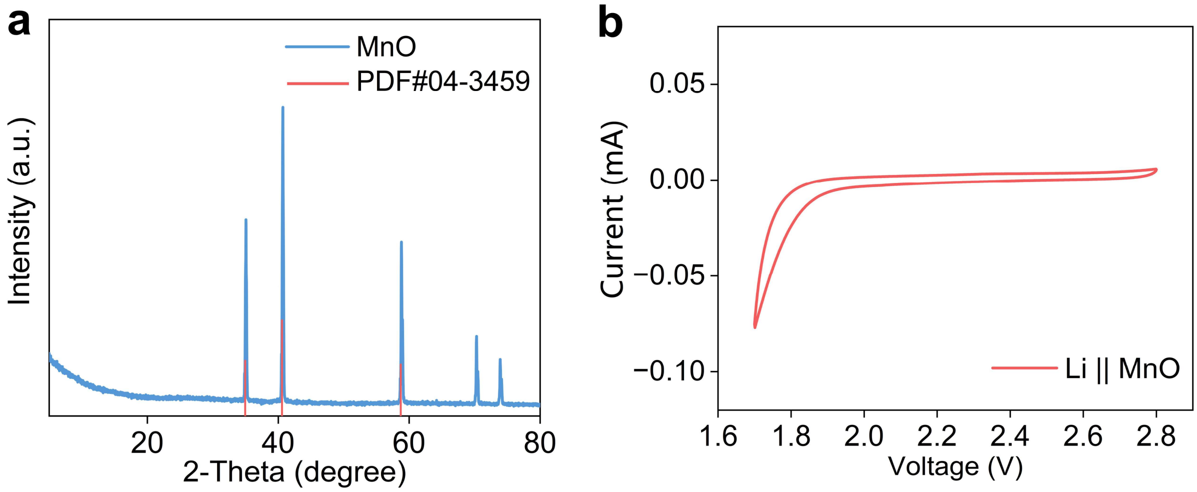

Supplementary Fig. 10 | The structural identification and electrochemical response of MnO. **a**, XRD pattern of MnO, showing good agreement with the standard diffraction peaks (PDF#04-3459) and confirming the crystalline phase of MnO. **b**, Cyclic voltammetry curve of MnO versus Li/Li$^+$, recorded over the indicated voltage window, revealing the electrochemical response of the MnO electrode in a lithium half-cell configuration.

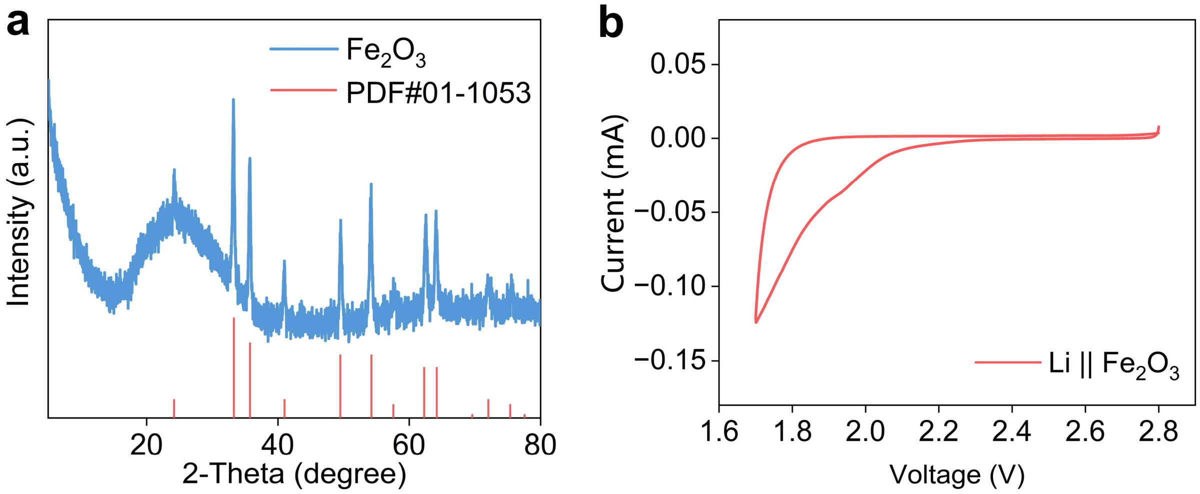

Supplementary Fig. 11 | The structural identification and electrochemical response of Fe_2O_3. **a**, XRD pattern of Fe_2O_3, showing good agreement with the standard diffraction peaks (PDF#01-1053) and confirming the crystalline phase of Fe_2O_3. **b**, Cyclic voltammetry curve of Fe_2O_3 versus Li/Li$^+$, recorded over the indicated voltage window, revealing the electrochemical response of the Fe_2O_3 electrode in a lithium half-cell configuration.

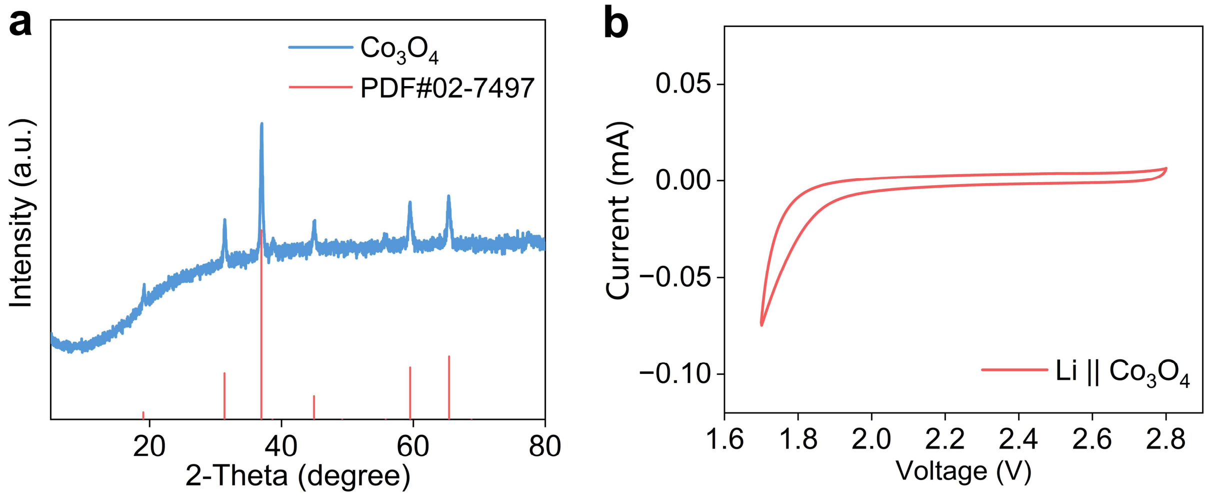

Supplementary Fig. 12 | The structural identification and electrochemical response of Co_3O_4. **a**, XRD pattern of Co_3O_4, showing good agreement with the standard diffraction peaks (PDF#02-7497) and confirming the crystalline phase of Co_3O_4. **b**, Cyclic voltammetry curve of Co_3O_4 versus Li/Li^+, recorded over the indicated voltage window, revealing the electrochemical response of the Co_3O_4 electrode in a lithium half-cell configuration.

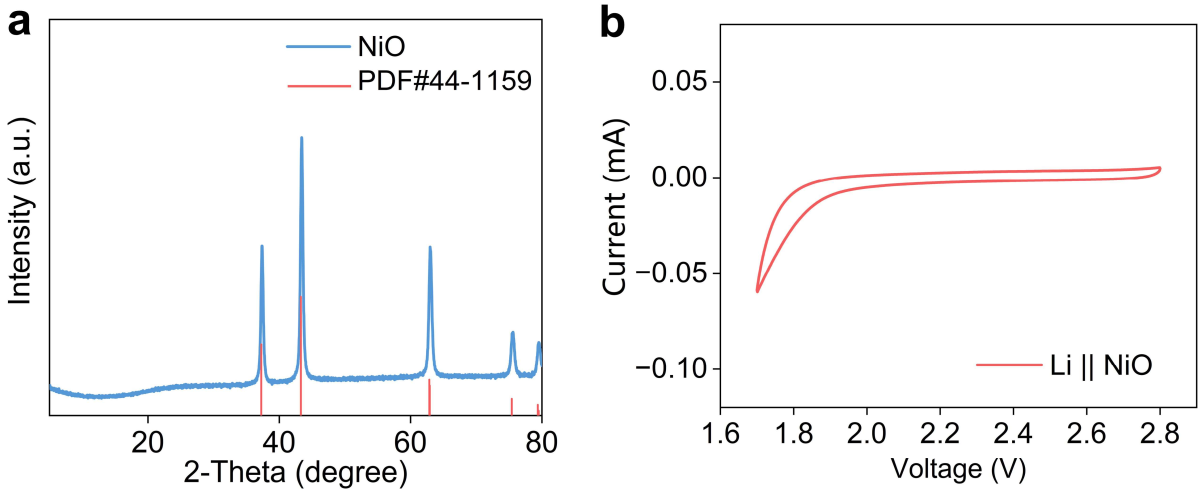

Supplementary Fig. 13 | The structural identification and electrochemical response of NiO. **a**, XRD pattern of NiO, showing good agreement with the standard diffraction peaks (PDF#44-1159) and confirming the crystalline phase of NiO. **b**, Cyclic voltammetry curve of NiO versus Li/Li$^+$, recorded over the indicated voltage window, revealing the electrochemical response of the NiO electrode in a lithium half-cell configuration.

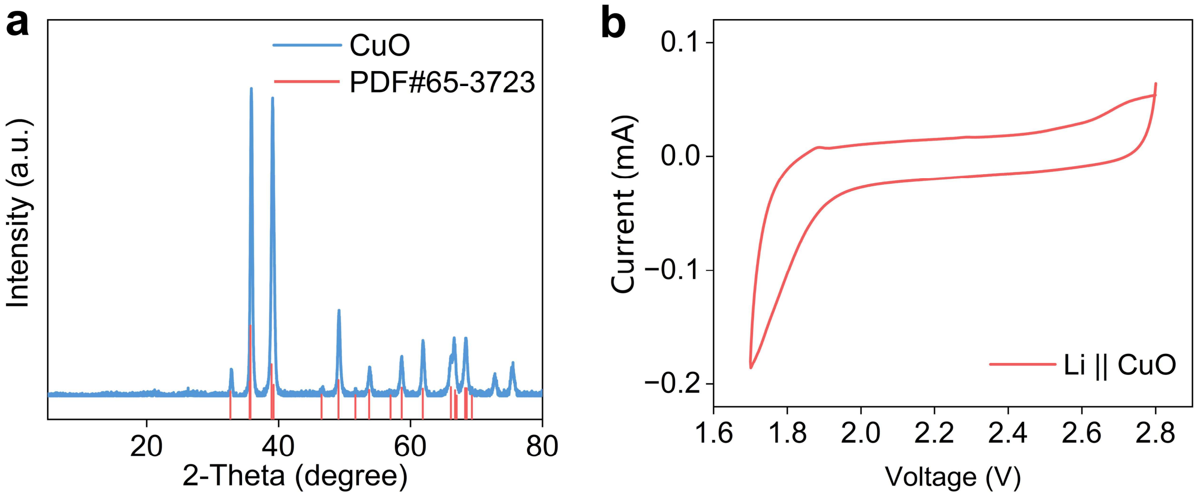

Supplementary Fig. 14 | The structural identification and electrochemical response of CuO. **a**, XRD pattern of CuO, showing good agreement with the standard diffraction peaks (PDF#65-3723) and confirming the crystalline phase of CuO. **b**, Cyclic voltammetry curve of CuO versus Li/Li$^+$, recorded over the indicated voltage window, revealing the electrochemical response of the CuO electrode in a lithium half-cell configuration.

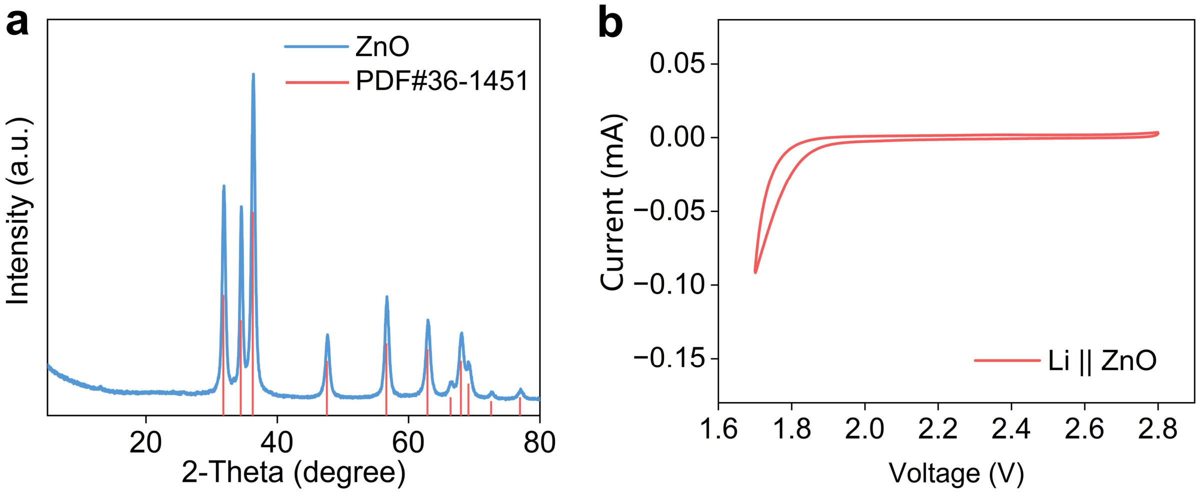

Supplementary Fig. 15 | The structural identification and electrochemical response of ZnO. **a**, XRD pattern of ZnO, showing good agreement with the standard diffraction peaks (PDF#36-1451) and confirming the crystalline phase of ZnO. **b**, Cyclic voltammetry curve of ZnO versus Li/Li$^+$, recorded over the indicated voltage window, revealing the electrochemical response of the ZnO electrode in a lithium half-cell configuration.

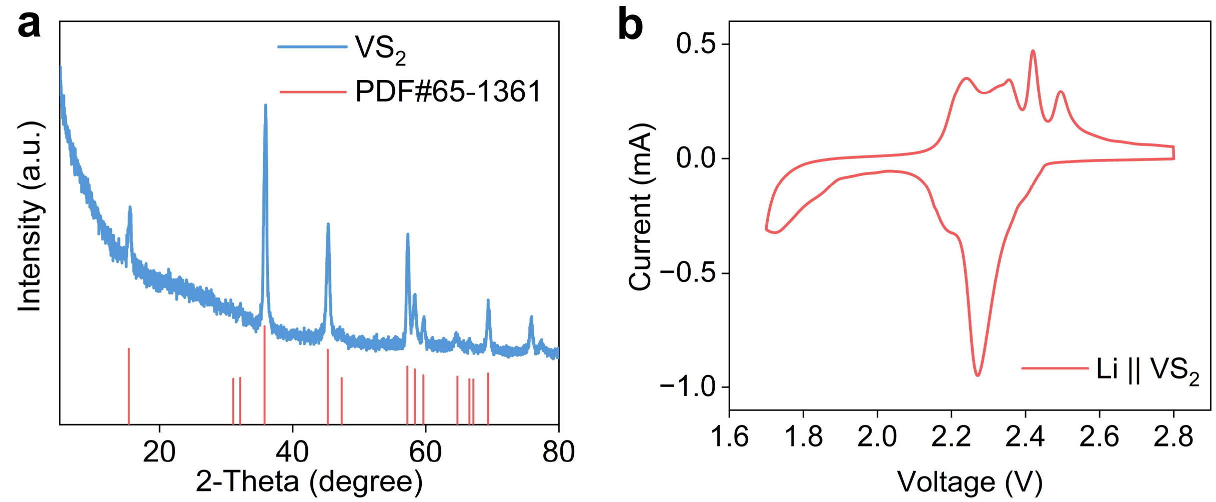

Supplementary Fig. 16 | The structural identification and electrochemical response of VS_2. **a**, XRD pattern of VS_2, showing good agreement with the standard diffraction peaks (PDF#65-1361) and confirming the crystalline phase of VS_2. **b**, Cyclic voltammetry curve of VS_2 versus Li/Li^+, recorded over the indicated voltage window, revealing the electrochemical response of the VS_2 electrode in a lithium half-cell configuration.

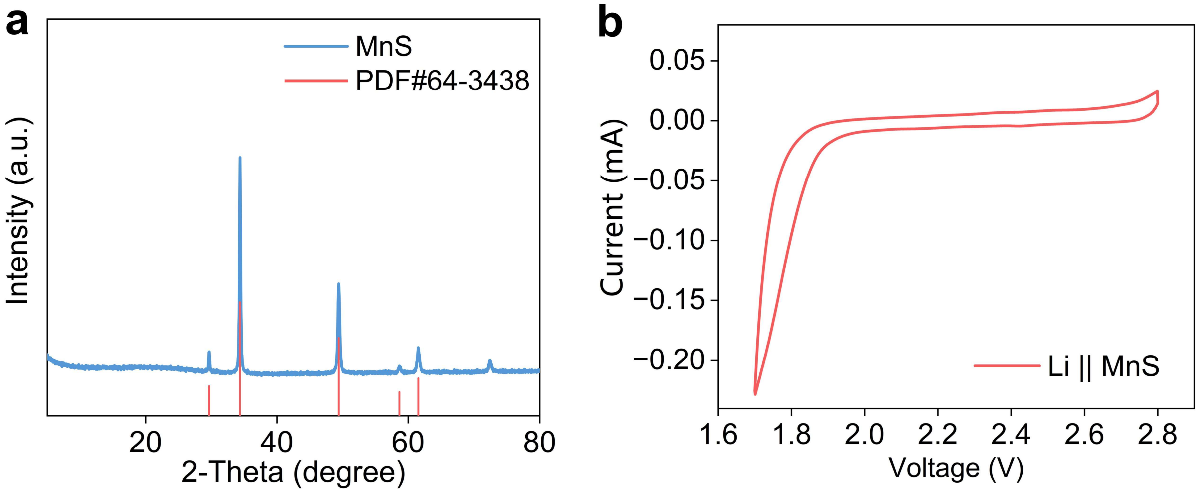

Supplementary Fig. 17 | The structural identification and electrochemical response of MnS. **a**, XRD pattern of MnS, showing good agreement with the standard diffraction peaks (PDF#64-3438) and confirming the crystalline phase of MnS. **b**, Cyclic voltammetry curve of MnS versus Li/Li$^+$, recorded over the indicated voltage window, revealing the electrochemical response of the MnS electrode in a lithium half-cell configuration.

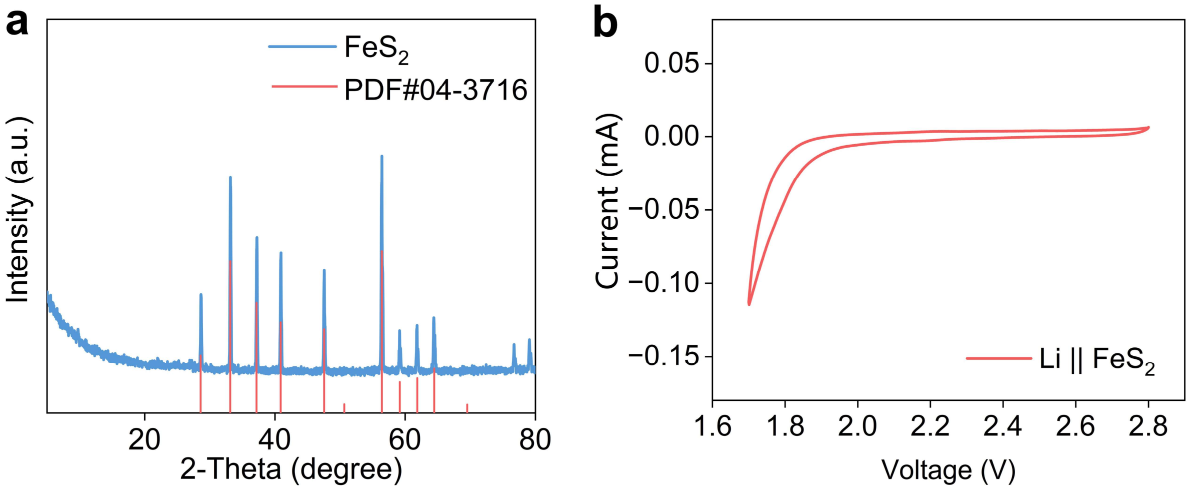

Supplementary Fig. 18 | The structural identification and electrochemical response of FeS_2. **a**, XRD pattern of FeS_2, showing good agreement with the standard diffraction peaks (PDF#04-3716) and confirming the crystalline phase of FeS_2. **b**, Cyclic voltammetry curve of FeS_2 versus Li/Li^+, recorded over the indicated voltage window, revealing the electrochemical response of the FeS_2 electrode in a lithium half-cell configuration.

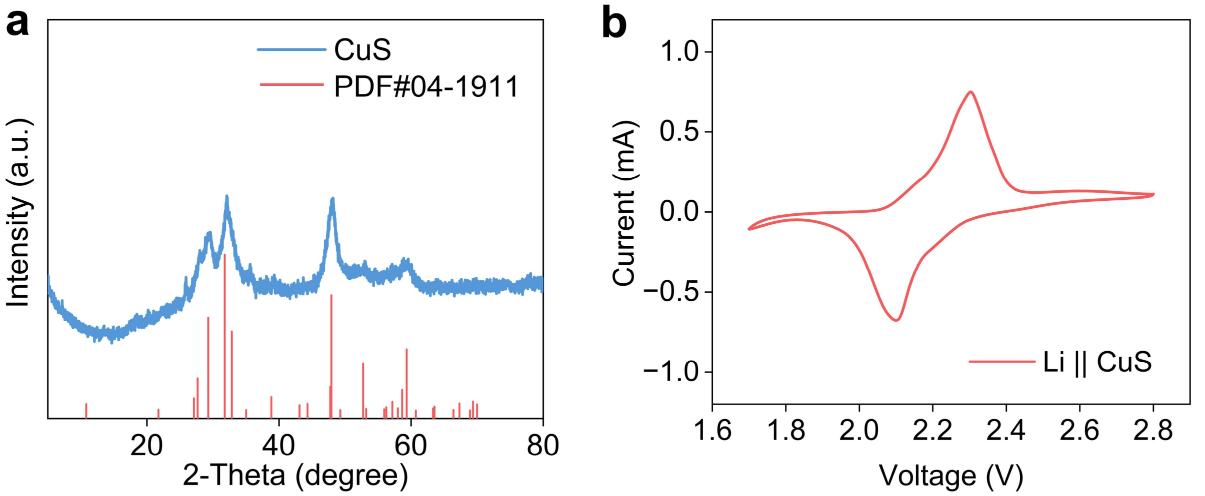

Supplementary Fig. 19 | The structural identification and electrochemical response of CuS. **a**, XRD pattern of CuS, showing good agreement with the standard diffraction peaks (PDF#04-1911) and confirming the crystalline phase of CuS. **b**, Cyclic voltammetry curve of CuS versus Li/Li^{+}, recorded over the indicated voltage window, revealing the electrochemical response of the CuS electrode in a lithium half-cell configuration.

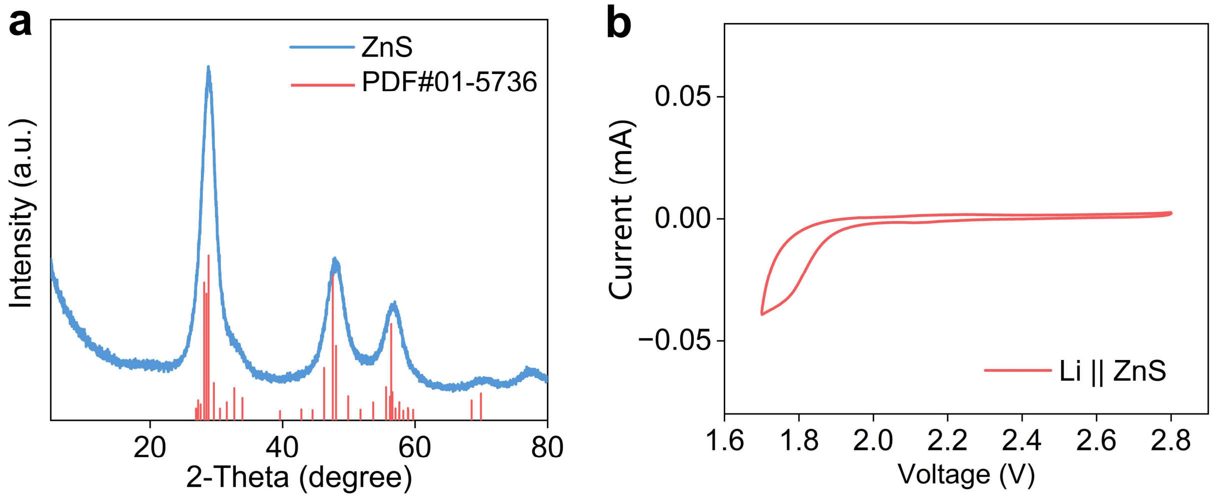

Supplementary Fig. 20 | The structural identification and electrochemical response of ZnS. **a**, XRD pattern of ZnS, showing good agreement with the standard diffraction peaks (PDF#01-5736) and confirming the crystalline phase of ZnS. **b**, Cyclic voltammetry curve of ZnS versus Li/Li$^+$, recorded over the indicated voltage window, revealing the electrochemical response of the ZnS electrode in a lithium half-cell configuration.

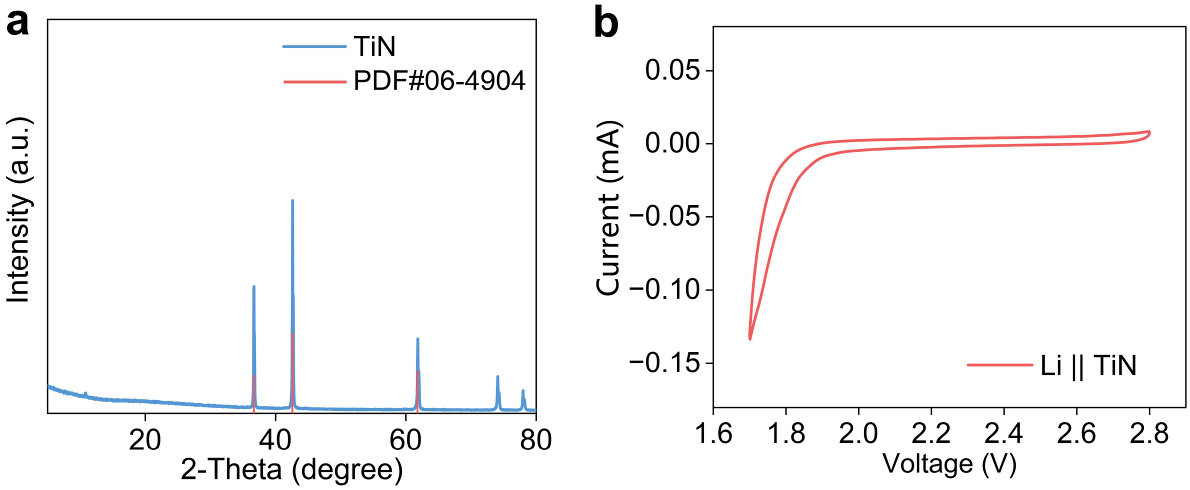

Supplementary Fig. 21 | The structural identification and electrochemical response of TiN. **a**, XRD pattern of TiN, showing good agreement with the standard diffraction peaks (PDF#06-4904) and confirming the crystalline phase of TiN. **b**, Cyclic voltammetry curve of TiN versus Li/Li$^+$, recorded over the indicated voltage window, revealing the electrochemical response of the TiN electrode in a lithium half-cell configuration.

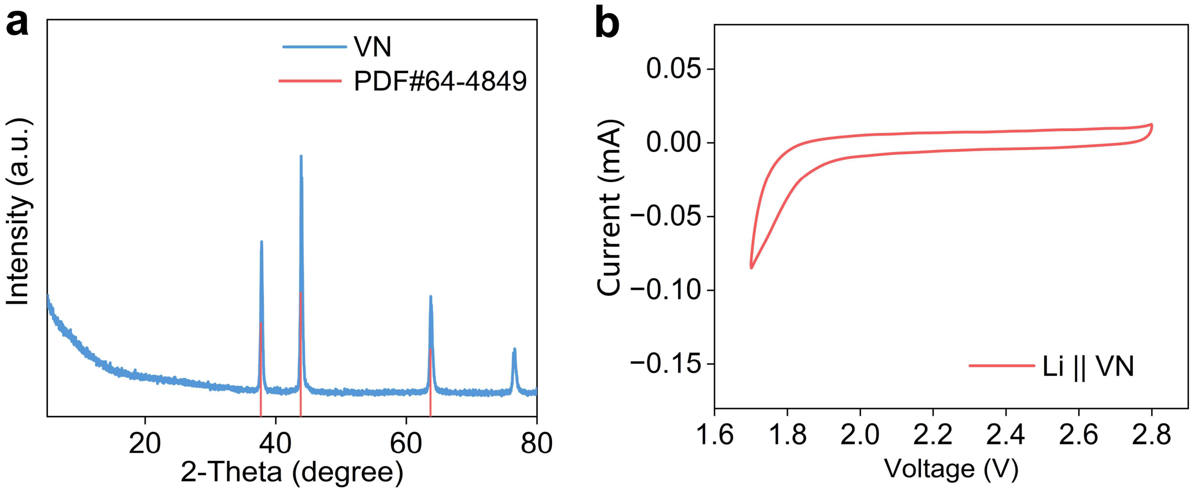

Supplementary Fig. 22 | The structural identification and electrochemical response of VN. **a**, XRD pattern of VN, showing good agreement with the standard diffraction peaks (PDF#64-4849) and confirming the crystalline phase of VN. **b**, Cyclic voltammetry curve of VN versus Li/Li$^+$, recorded over the indicated voltage window, revealing the electrochemical response of the VN electrode in a lithium half-cell configuration.

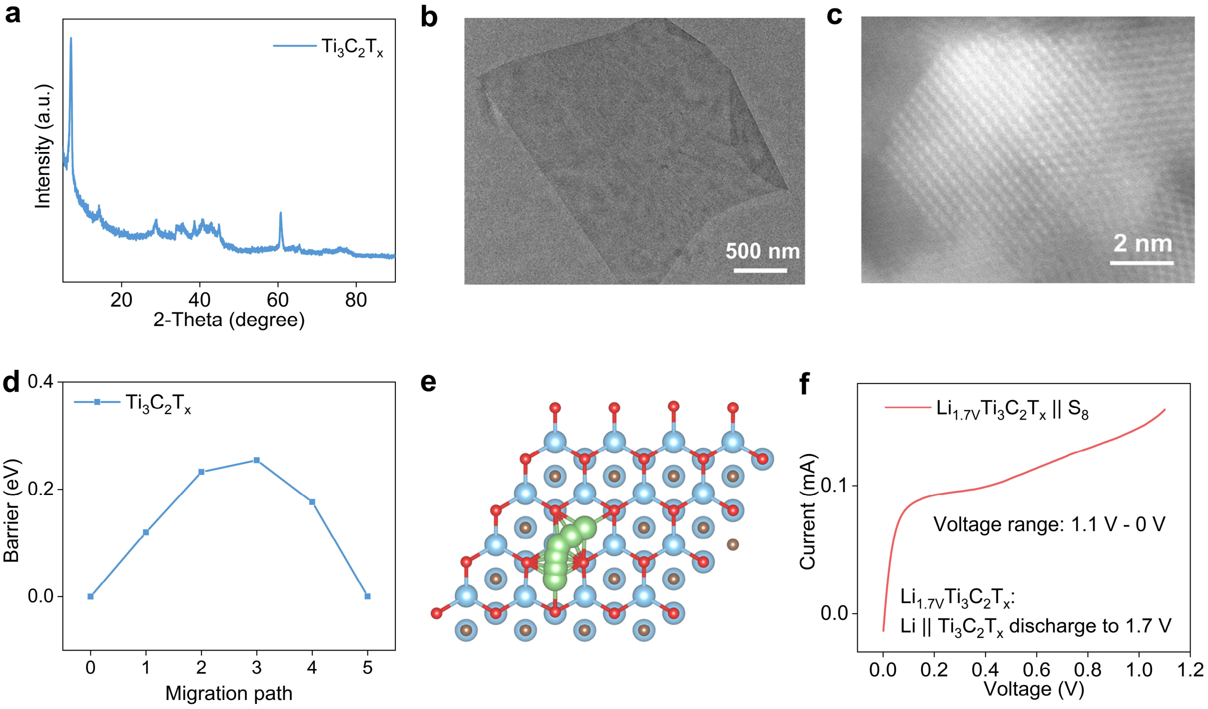

Supplementary Fig. 23 | Synthesis of $Ti_3C_2T_x$ and characterization of its lithiation behavior. **a**, The appearance of the characteristic (002) reflection at ~7°, along with additional peaks consistent with literature reports, confirms the successful preparation of the material. **b**, The low-magnification TEM image. **c**, The aberration-corrected scanning transmission electron microscopy (STEM) image. **d**,**e**, The calculated diffusion barriers for Li^+ on $Ti_3C_2T_x$. **f**, Validation of the lithium-reservoir strategy. The Li||$Ti_3C_2T_x$ cell exhibits an open-circuit voltage of ~3.0 V; after discharging to 1.7 V, $Ti_3C_2T_x$ becomes lithiated, forming $Li_{1.7V}Ti_3C_2T_x$. This material is then employed as the anode in a $Li_{1.7V}Ti_3C_2T_x$||S_8 cell, whose theoretical open-circuit voltage is ~1.1 V. CV performed between 1.1 and 0.01 V at a scan rate of 0.2 mV s^{-1} reveals a distinct reduction peak, confirming the viability of the lithium-reservoir strategy in practical systems.

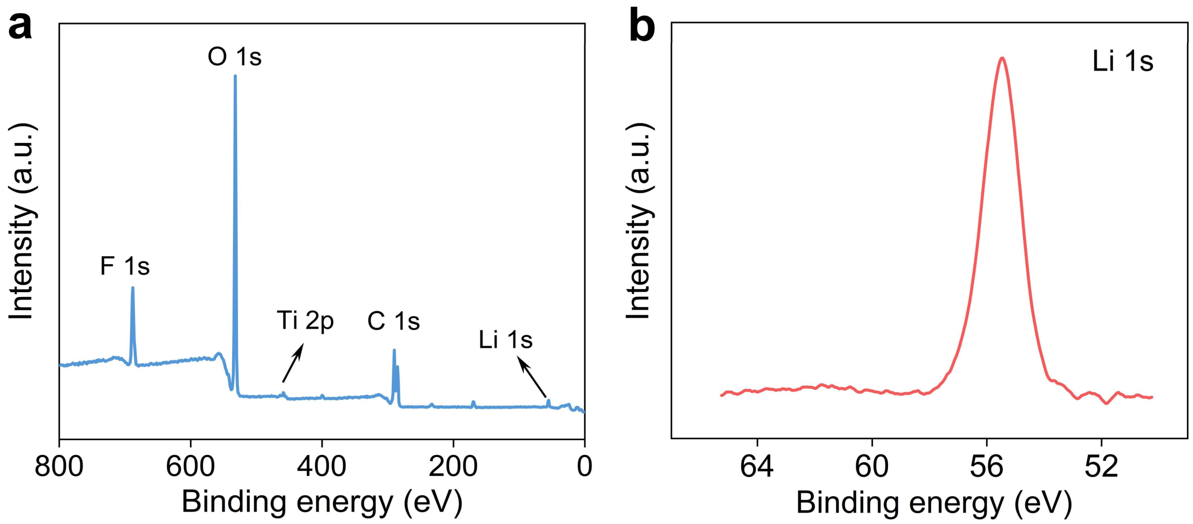

Supplementary Fig. 24 | The XPS characterization of $Ti_3C_2T_x$ lithium storage performance. **a**, XPS spectrum of $Ti_3C_2T_x$ after lithium storage. **b**, High-resolution XPS spectrum of Li 1s.

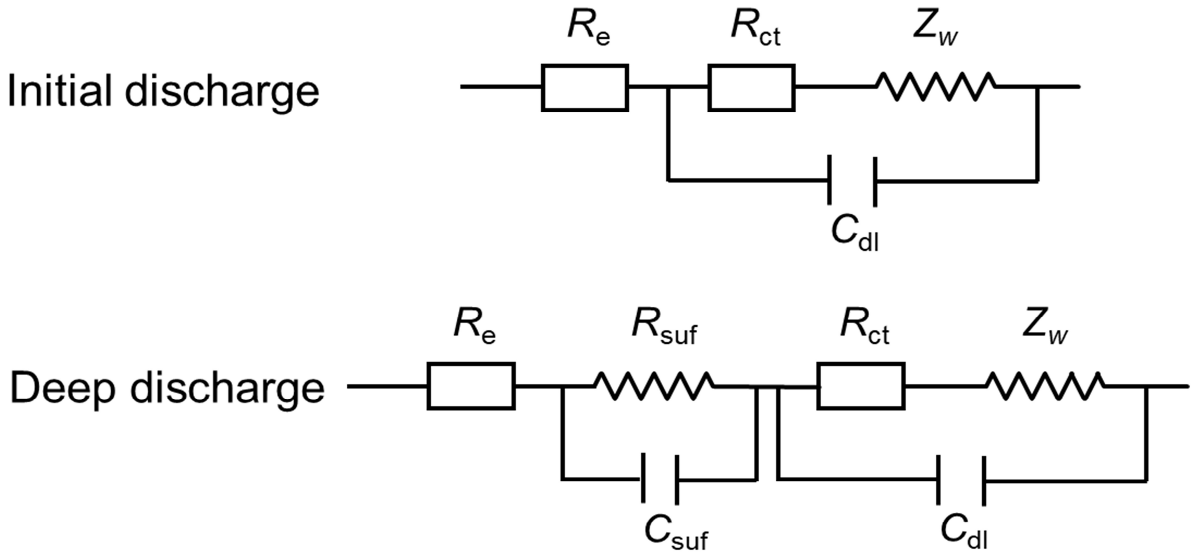

Supplementary Fig. 25 | Modeling LSB equivalent circuits for the initial discharge and deep discharge. R_e represents internal electrolyte resistance, R_{ct} denotes charge–transfer resistance, and R_{suf} signifies electrolyte/electrode interface resistance. Z_W reflects Warburg diffusion impedance.

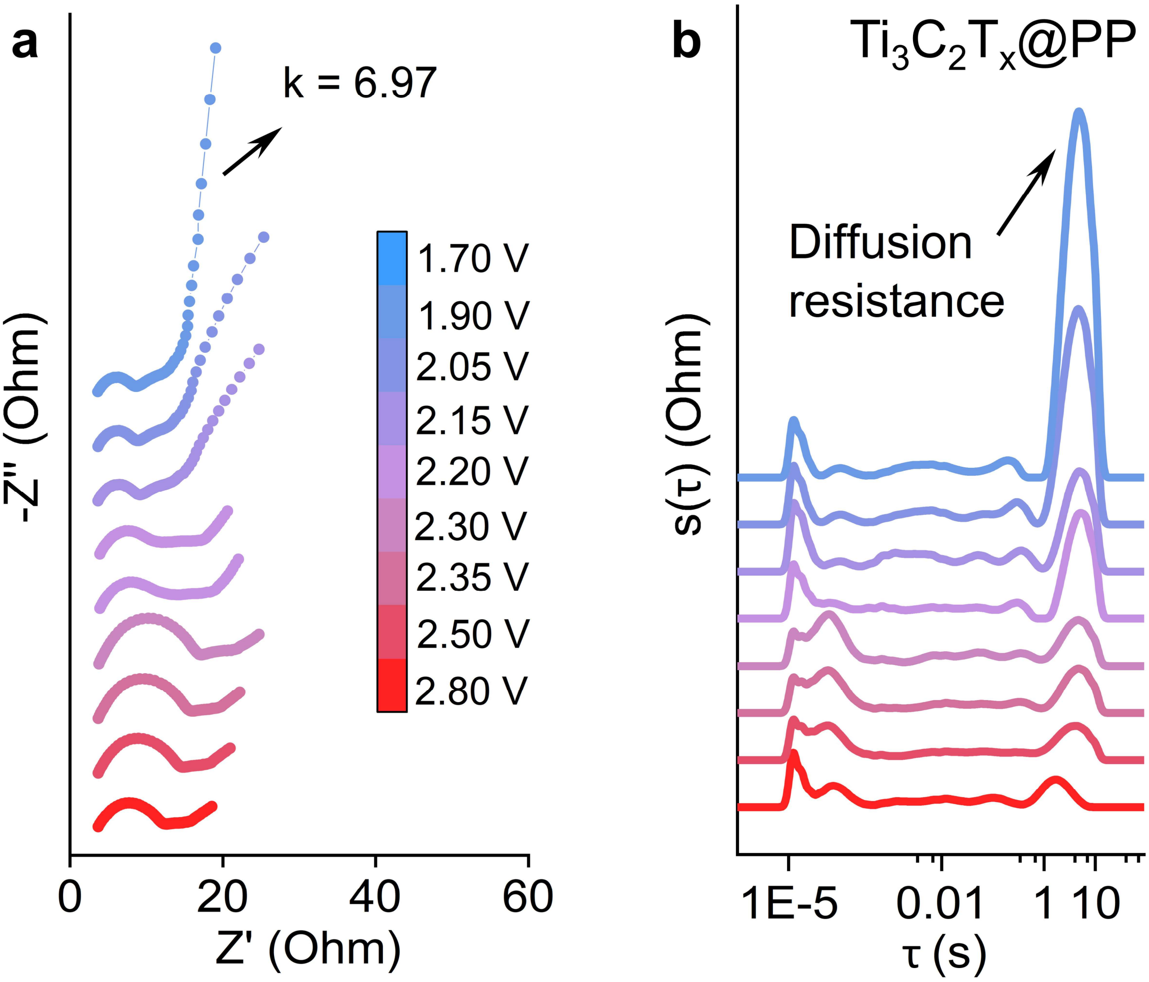

Supplementary Fig. 26 | In situ electrochemical impedance spectroscopy and time-domain relaxation analysis of LSBs assembled with $Ti_3C_2T_x$ @PP. a, In–situ EIS of LSBs assembled with $Ti_3C_2T_x$@PP. **b**, Time relaxation analysis of electrochemical impedance to evaluation of lithium–ion mass transfer kinetics.

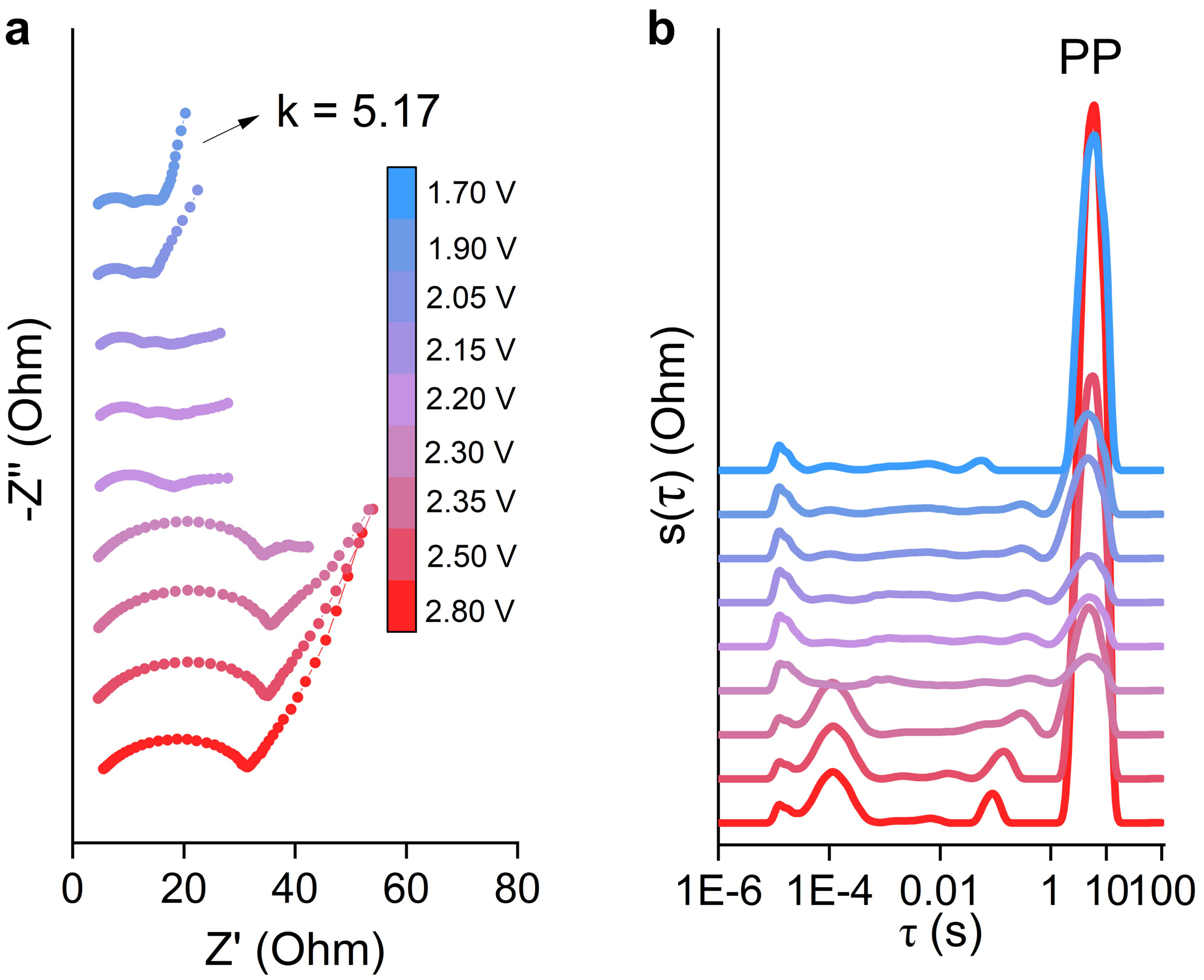

Supplementary Fig. 27 | In situ electrochemical impedance spectroscopy and time-domain relaxation analysis of LSBs assembled with PP. a, In–situ EIS of LSBs assembled with PP. **b**, Time relaxation analysis of electrochemical impedance to evaluation of lithium–ion mass transfer kinetics.

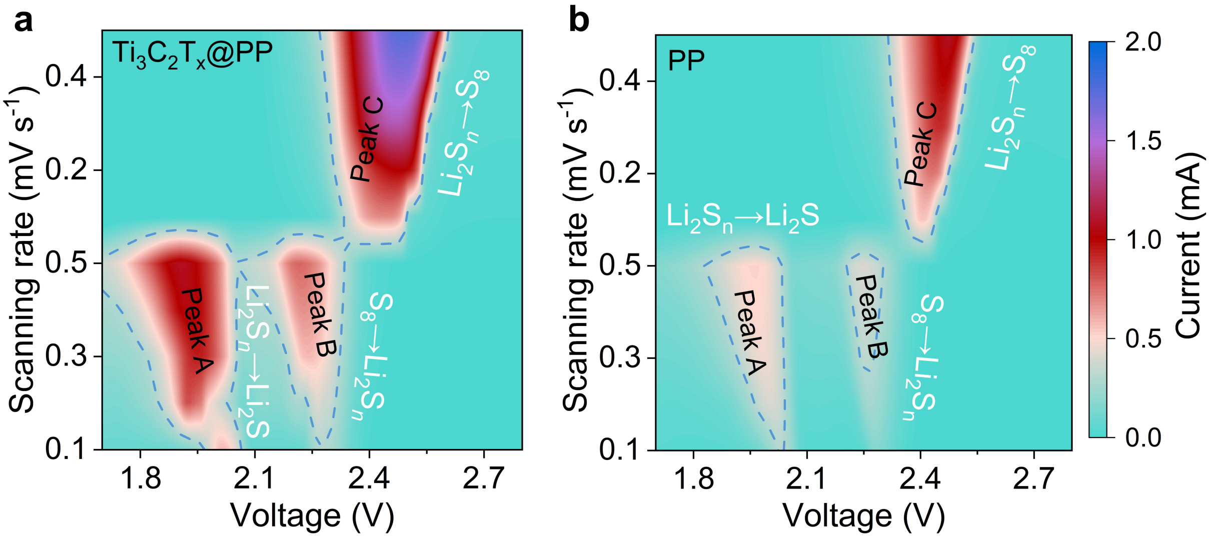

Supplementary Fig. 28 | Scan-rate-resolved kinetic landscape of multistep sulfur redox reactions. **a**, In–situ electrochemical impedance spectroscopy of LSBs assembled with $Ti_3C_2T_x$@PP. **b**, In–situ electrochemical impedance spectroscopy of LSBs assembled with PP.

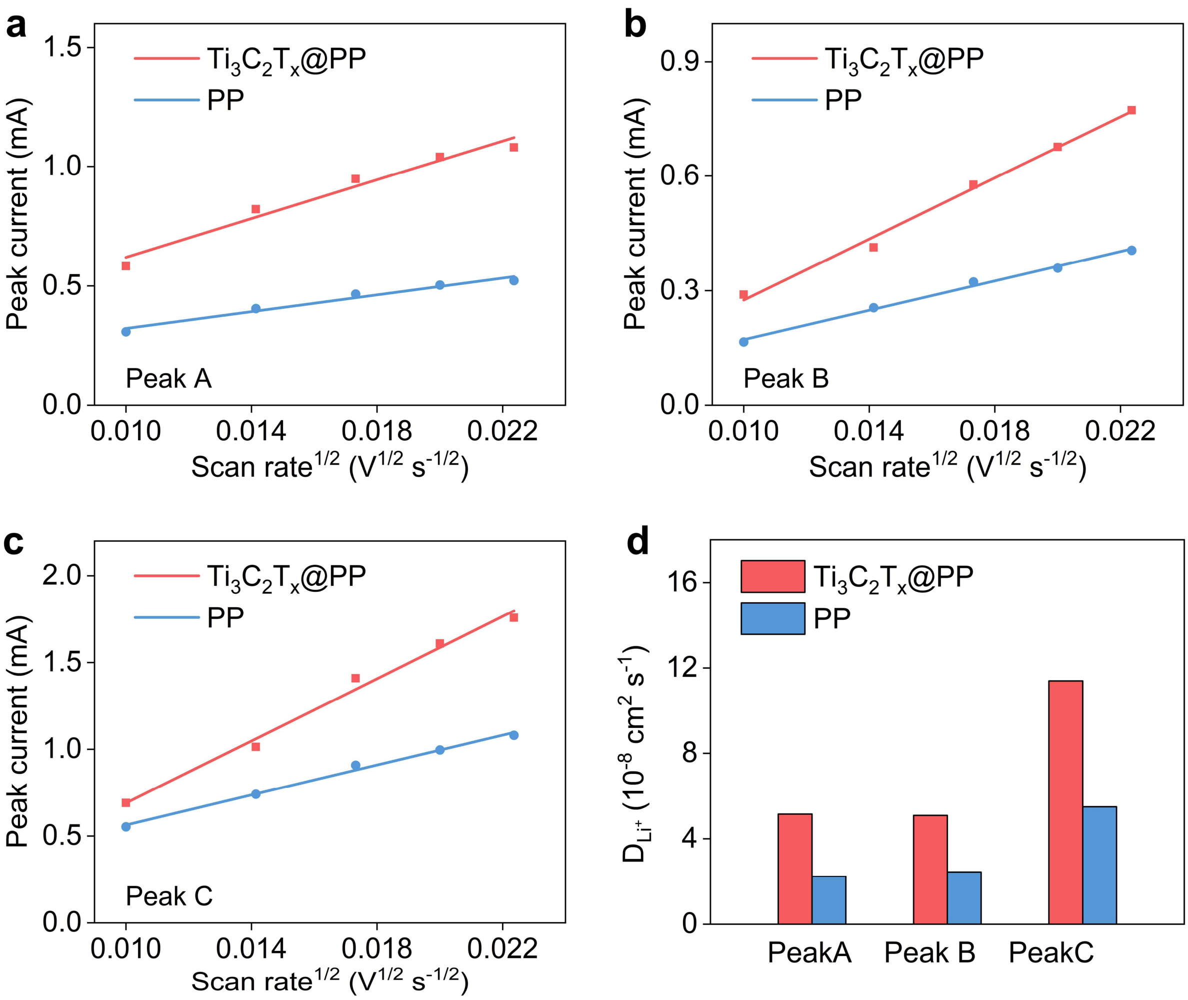

Supplementary Fig. 29 | Quantitative extraction of lithium-ion diffusion coefficients. a–**c**, The D_{Li+} for Peak A, B, and C fitted according to Randless–Sevcik equation in LSBs. **d**, Comparison of lithium-ion diffusion coefficients corresponding to the three peaks.

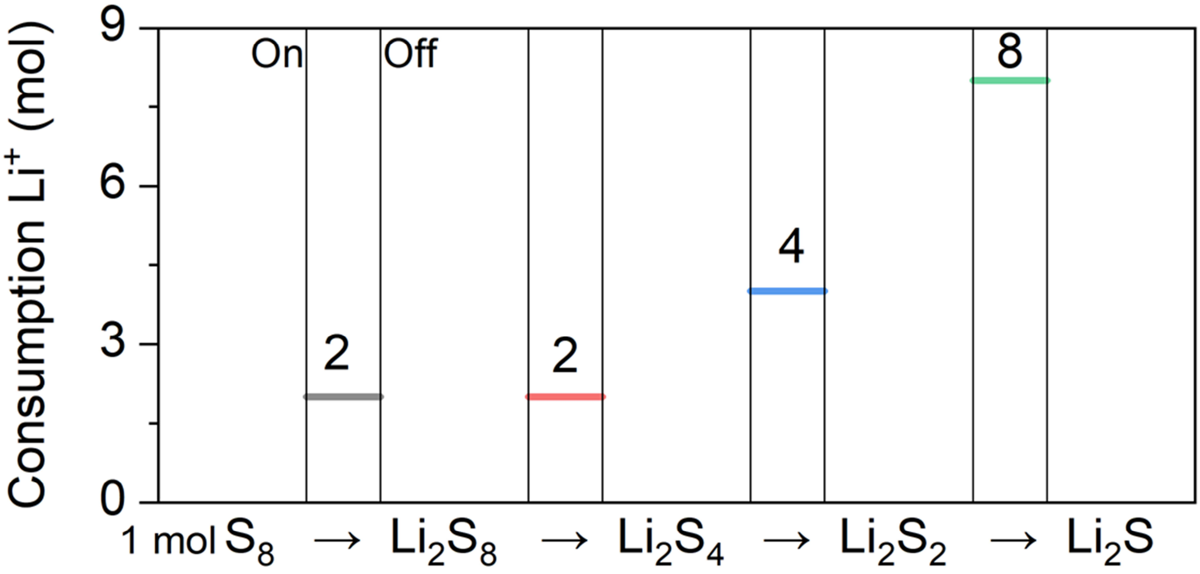

Supplementary Fig. 30 | The amount of Li^+ required for the complete conversion of 1 mol of S_8 to Li_2S at various stages of the SRR. From this, it can be observed that in the initial stage of SRR, the consumption of lithium ions is relatively low. However, during the nucleation phase, especially in the formation of Li_2S, a significant amount of lithium ions is consumed.

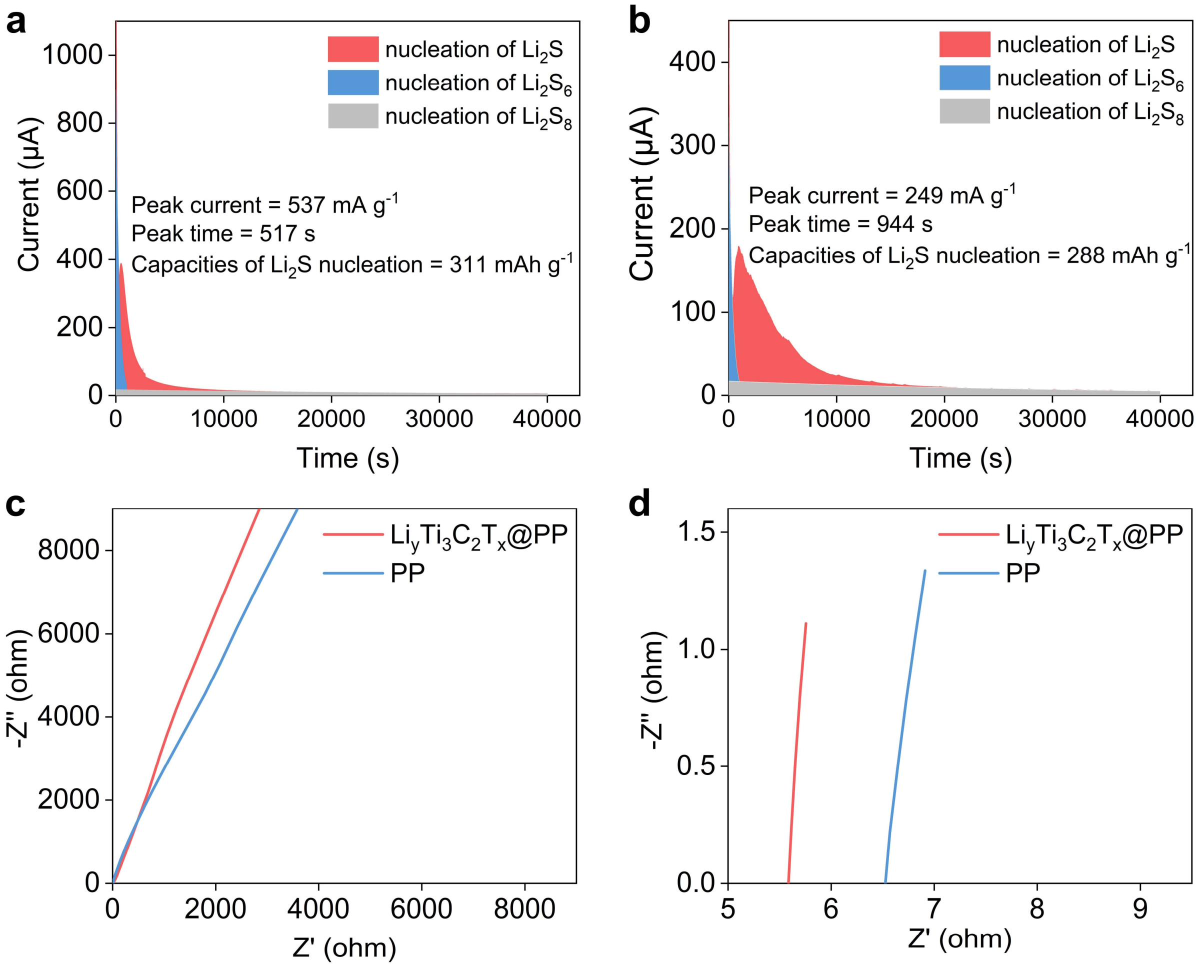

Supplementary Fig. 31 | Li_2S nucleation measurements and lithium-ion conductivity evaluation. a,**b**, respectively depict nucleation tests of batteries assembled with $Ti_3C_2T_x$ @PP and PP. **c**, Impedance spectra of Li–Li symmetric cells assembled with $Ti_3C_2T_x$@PP and PP separators. **d**, A magnified view of panel C.

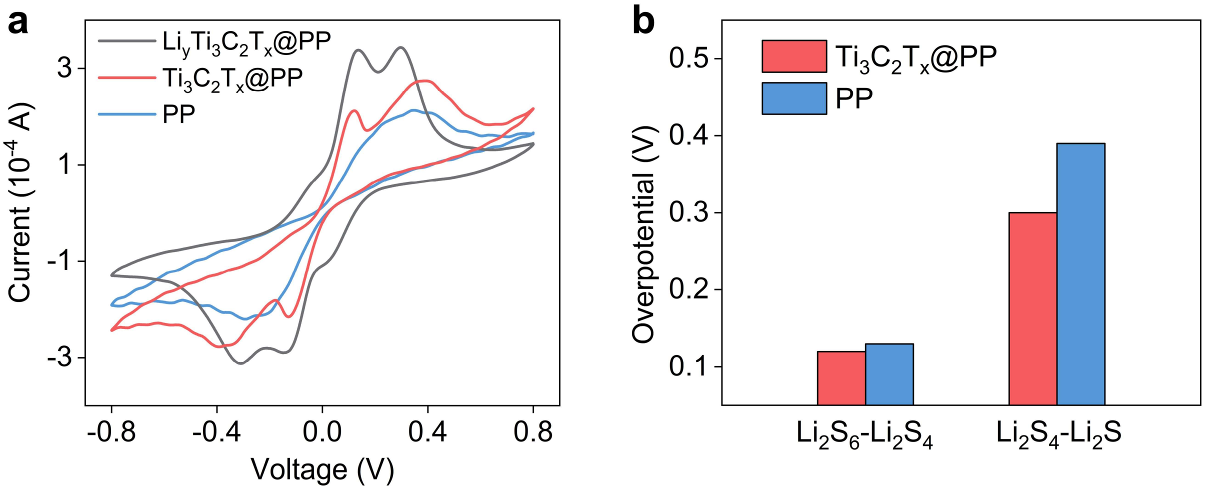

Supplementary Fig. 32 | Electrochemical polarization behavior of prelithiated and unlithiated $Ti_3C_2T_x$@PP. a,**b**, Compares the CV curves of a pre-lithiated $Li_yTi_3C_2T_x$@PP with an unlithiated $Ti_3C_2T_x$@PP. The redox pair near 0.1 V arises from the conversion of liquid polysulfides, and both systems display comparable polarization. In contrast, for the second redox pair around 0.4 V, the unlithiated $Ti_3C_2T_x$ separator case shows markedly higher polarization because it cannot supply Li^+, whereas the pre-lithiated $Li_yTi_3C_2T_x$ separator counterpart exhibits substantially reduced polarization—directly demonstrating the reservoir's role in sustaining local lithium availability.

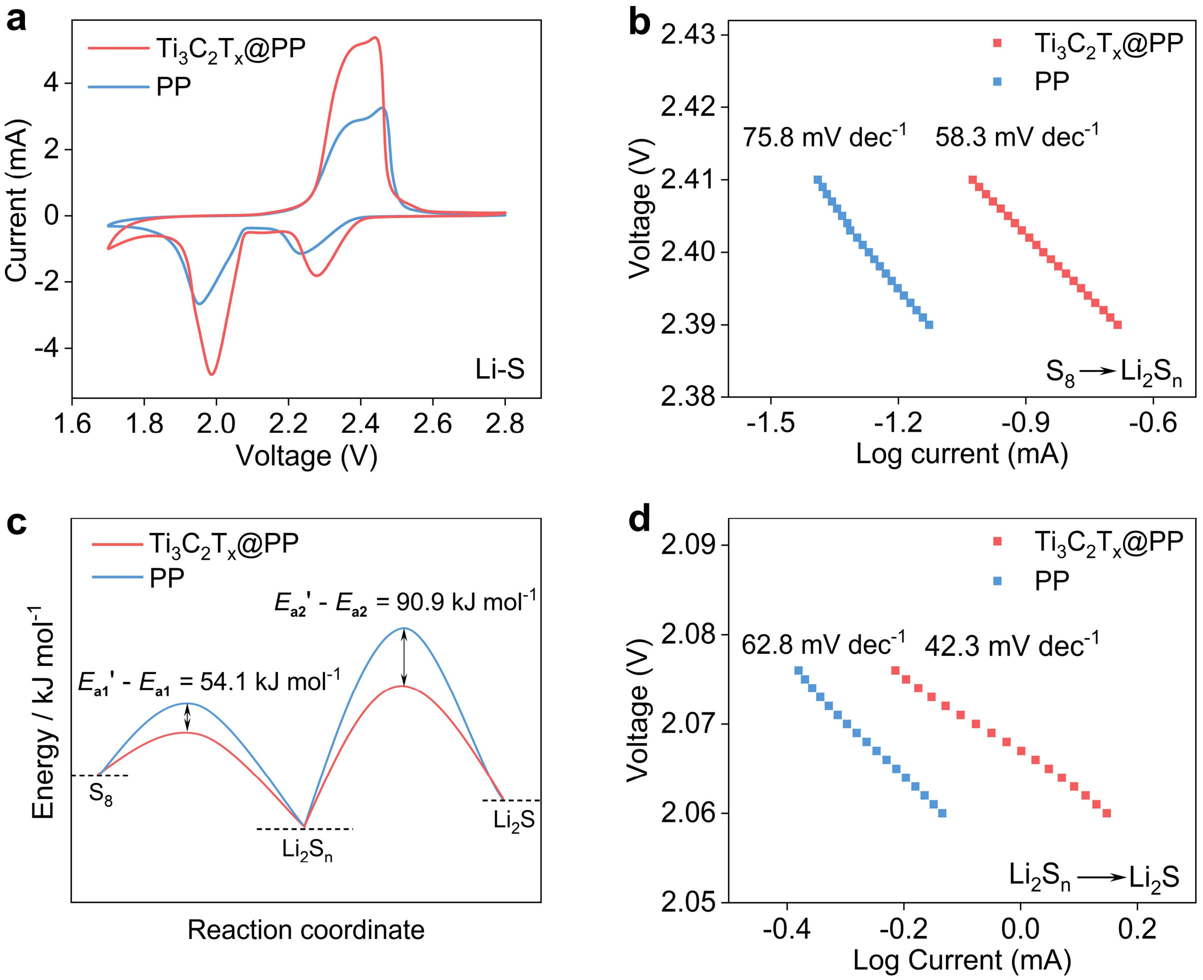

Supplementary Fig. 33 | CV and Tafel curves of LSBs. a, CV curves of lithium–sulfur cells assembled with $Ti_3C_2T_x$@PP and PP. **b**,**d**, present Tafel fitting of peaks at ~2.4 V and ~2.1 V in the discharge profiles from panel (**a**), with the derived activation energies shown in panel (**c**). This activation energy reflects the sum of the charge-transfer and ion-migration activation barriers. The results show that the apparent activation energy during the nucleation stage is substantially lower than that for the liquid–liquid polysulfide conversion process, indirectly confirming that the lithium-reservoir strategy effectively accelerates ion migration during the reaction.

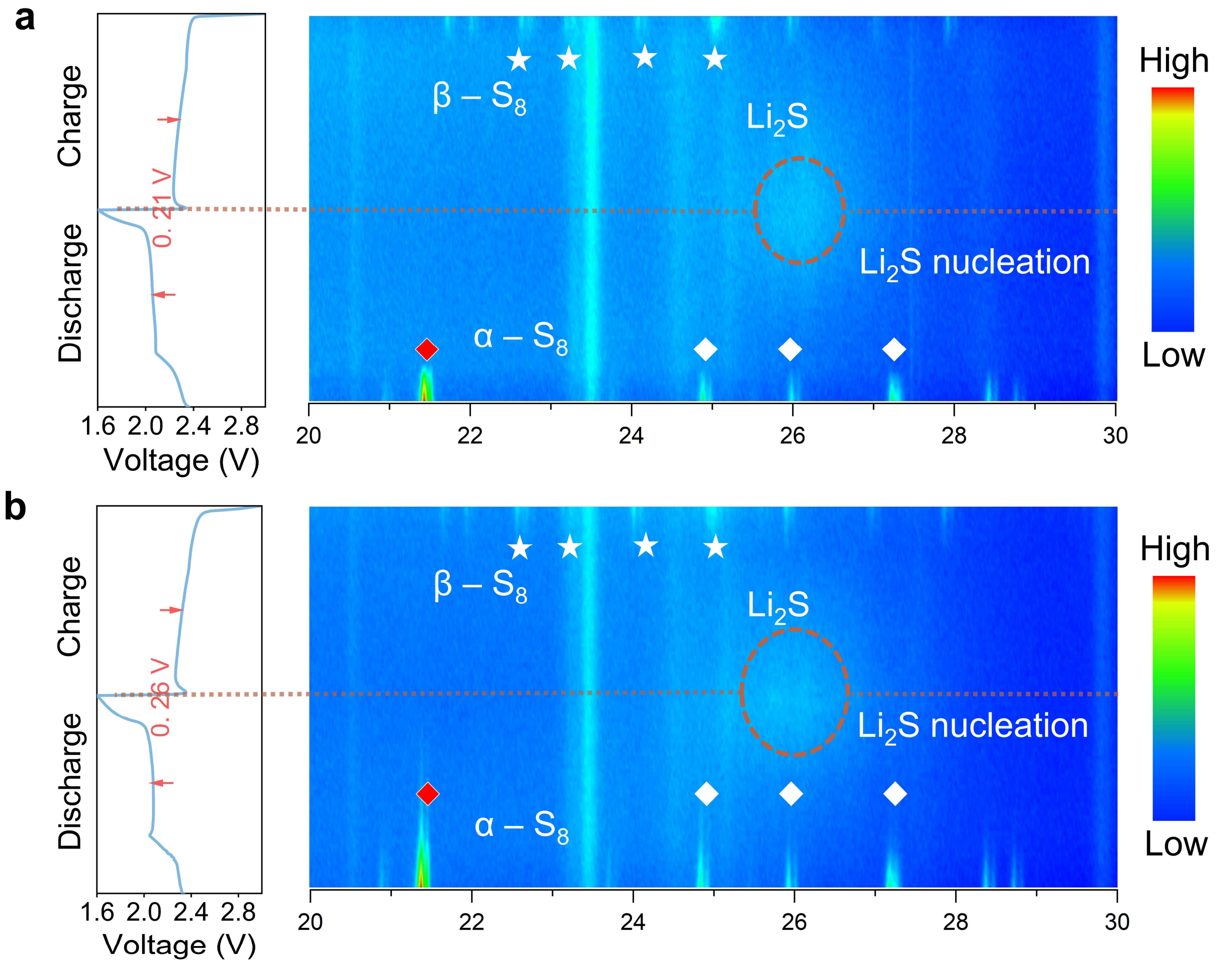

Supplementary Fig. 34 | In–situ XRD testing of LSBs with (a) $Ti_3C_2T_x$@PP and (b) PP. The $Ti_3C_2T_x$-modified system exhibits markedly faster Li_2S nucleation and decomposition, accompanied by reduced voltage polarization, indicating that the lithium-reservoir strategy substantially accelerates sulfur conversion kinetics.

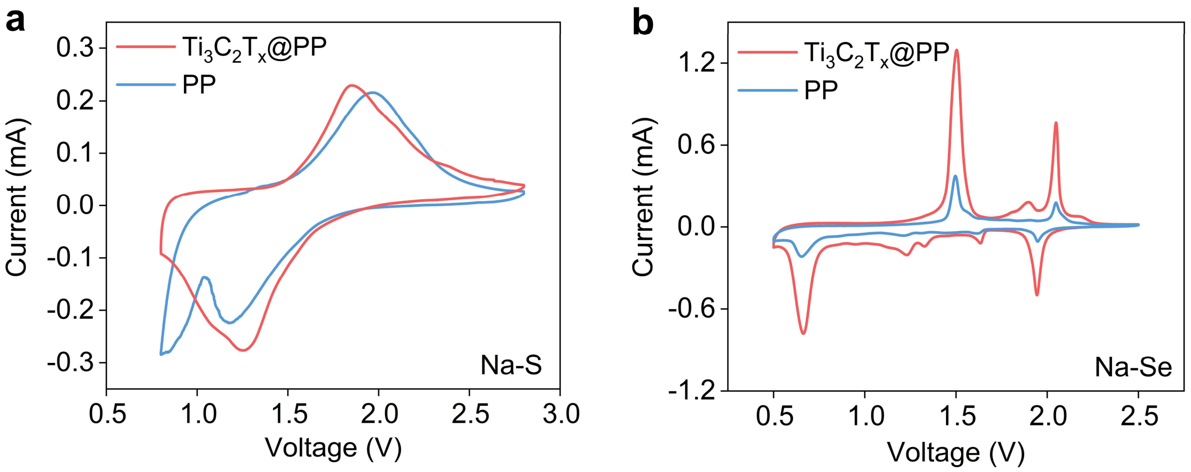

Supplementary Fig. 35 | CV curves of alkali metal–chalcogen batteries. a, Na–S batteries. **b**, Na–Se batteries.

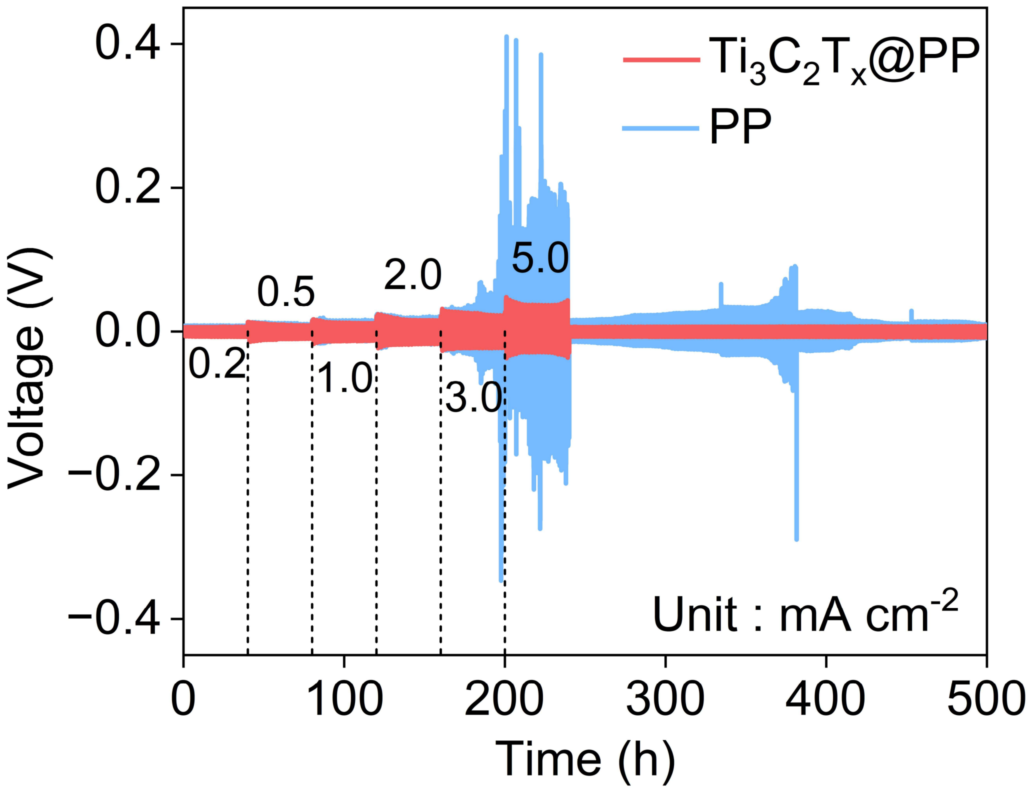

Supplementary Fig. 36 | Performance evaluation of the lithium anode. Rate performance as the current density increases from 0.2 to 5.0 mA cm^{-1} for both systems.

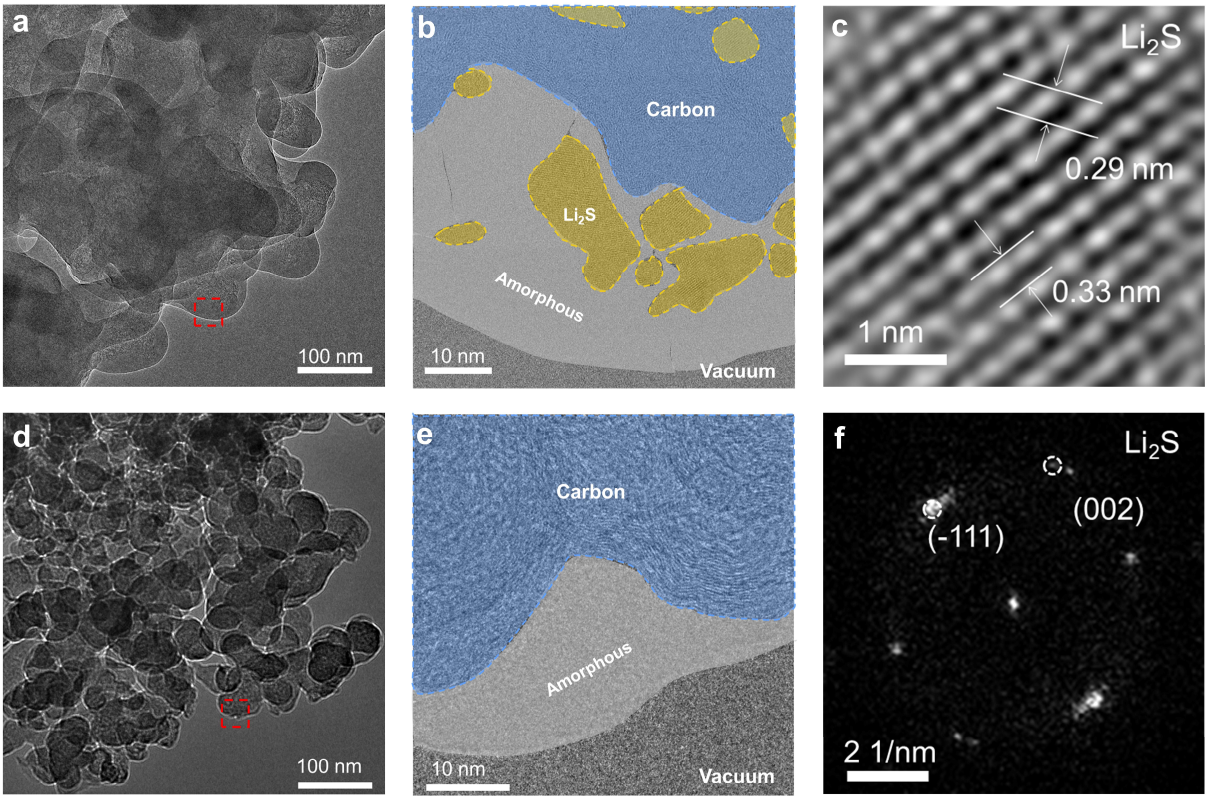

Supplementary Fig. 37 | Cryo-electron microscopy characterization of the sulfur cathode. a, Cryo-electron microscopy image of the cathode from a lithium–sulfur cell assembled with a conventional PP separator after one full discharge–charge cycle. **b**, A magnified view from panel A. The corresponding (**c**) lattice fringes and (**f**) electron diffraction pattern. The cathode of the cell employing a $Ti_3C_2T_x$-modified separator is shown in (**d**). The enlarged image in (**e**) reveals a far more preserved surface: the carbon framework remains sharply defined, and the CEI appears smooth and continuous, with no substantial Li_2S accumulation. It should be noted that organic-solvent rinsing during sample preparation dissolves native sulfur species. Abundant residues of incompletely decomposed Li_2S remain on the carbon matrix and within the cathode–electrolyte interphase in (**b**).

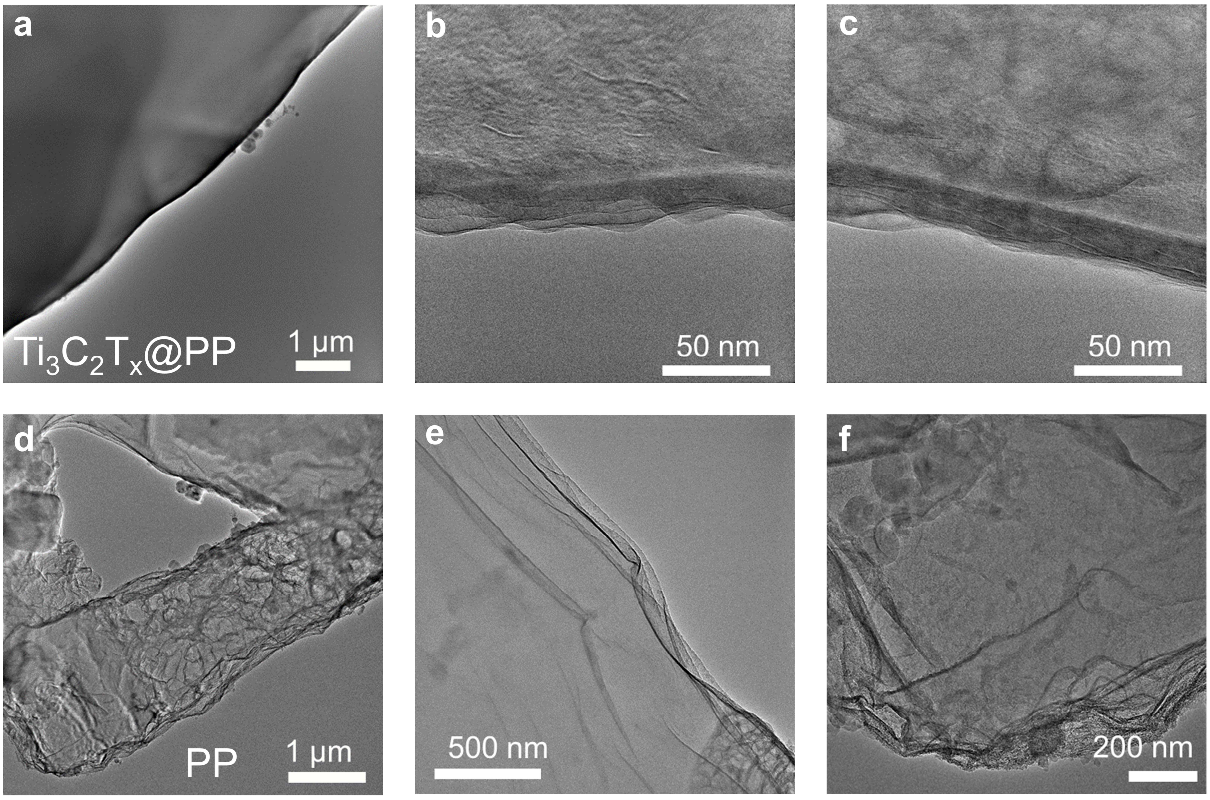

Supplementary Fig. 38 | Cryo-electron microscopy characterization of the lithium anode. **a**, Cryo-electron microscopy image of the lithium anode in the $Ti_3C_2T_x$-modified separator cell after one full discharge–charge cycle. **b**,**c**, Magnified views of panel A, showing a continuous and smooth SEI composed predominantly of Li_2O and enriched with abundant lithium vacancies, which facilitate rapid Li^+ insertion and extraction. **d**–**f**, Cryo-electron microscopy images of the anode in the cell employing a conventional PP separator, revealing a wrinkled and fragmented SEI with complex compositions.

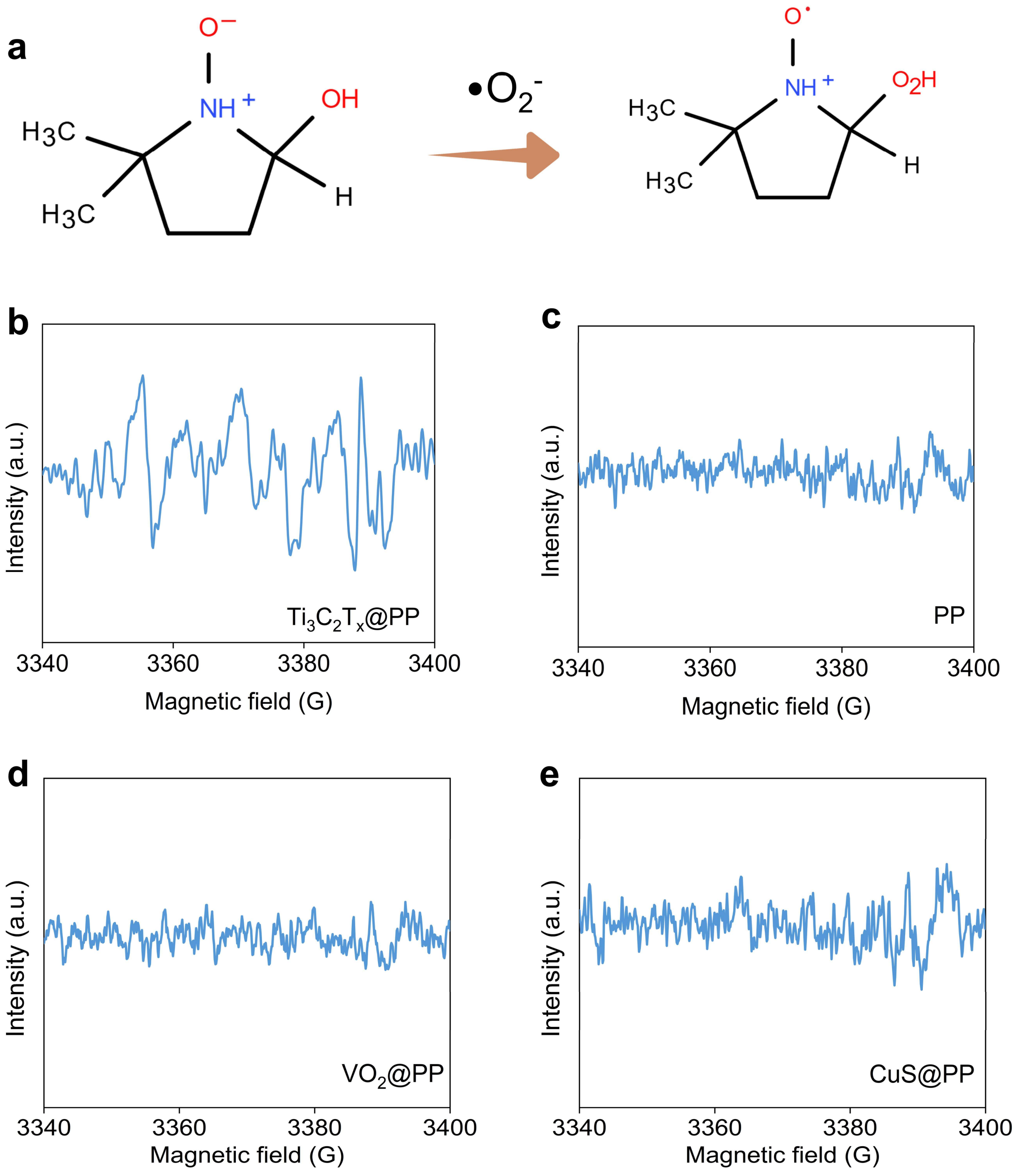

Supplementary Fig. 39 | Detection of superoxide radicals. a, Formation of DMPO–OH after trapping superoxide radicals with DMPO. **b**, Electron paramagnetic resonance spectra of the electrolyte from a $Ti_3C_2T_x$@PP-based lithium–sulfur pouch cell after cycling, exhibiting the characteristic six-line splitting of DMPO–OH. **c**–**e**, Electron paramagnetic resonance spectra of electrolytes from lithium–sulfur pouch cells assembled with PP, VO_2@PP, and CuS@PP separators, respectively, where no discernible radical signals are observed.

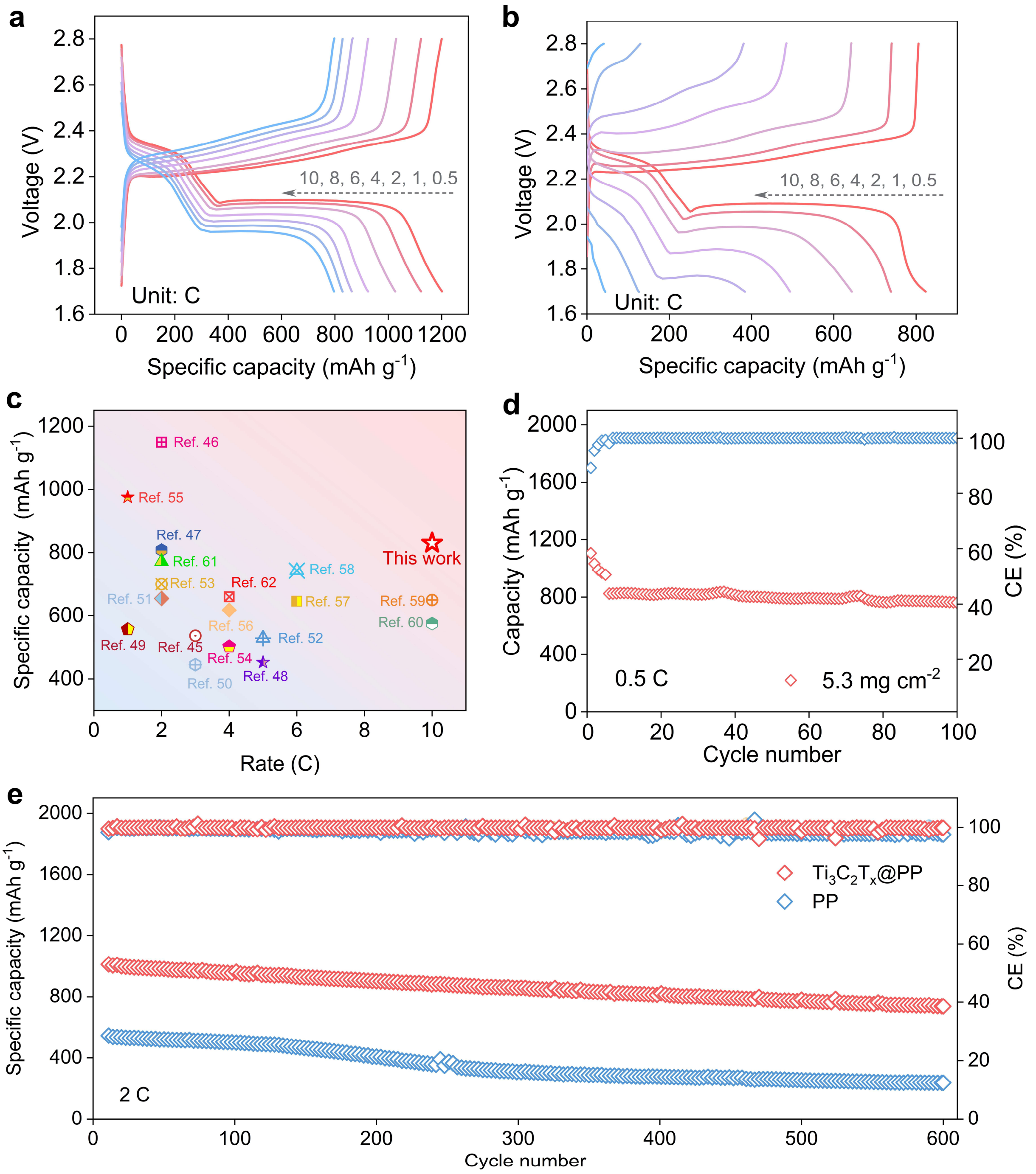

Supplementary Fig. 40 | Performance of LSBs. a,**b**, Rate-performance of LSBs assembled with $Ti_3C_2T_x$@PP and PP, respectively. **c**, Comparison of the rate performance of the LSBs in this study with previously reported systems. **d**, Cycling performance of a high-loading cell with an areal sulfur loading of 5.3 mg cm^{-1} at 0.5 C. **e**, Cycling performance of LSBs assembled with $Ti_3C_2T_x$@PP and PP at 2 C.

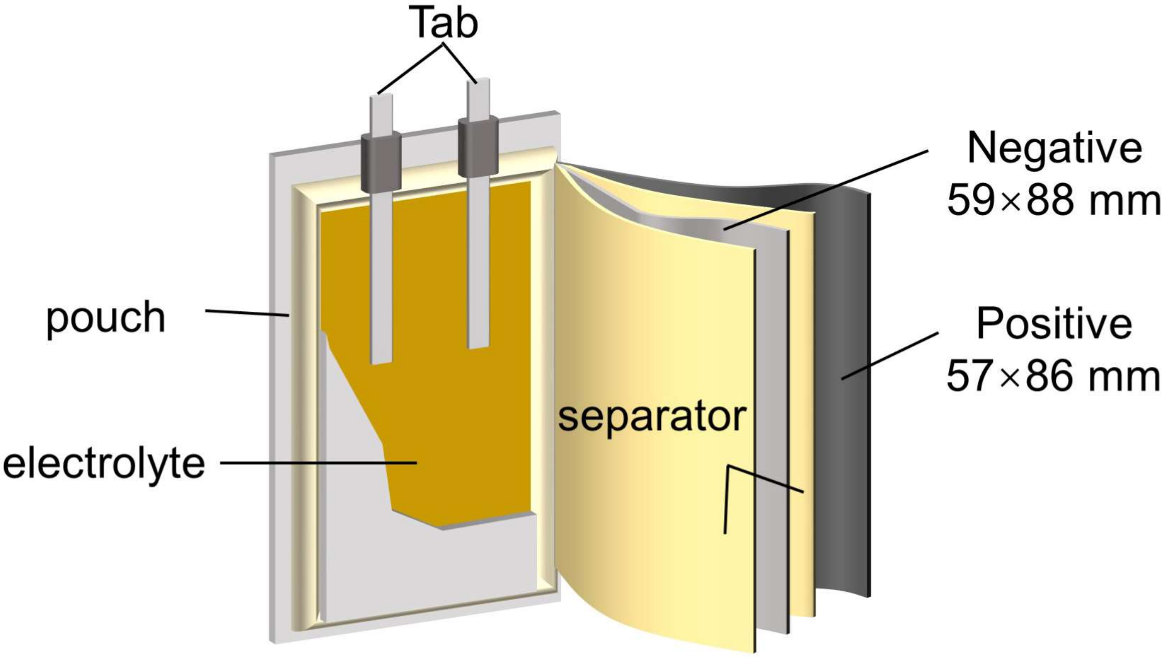

Supplementary Fig. 41 | Schematic diagram of the pouch battery structure. The sulfur areal loading is 7.5 mg cm^{-1}, utilizing two single-sided cathodes and three double-sided cathodes.

Supplementary Table 1. Solving the conservation equation for Li_2S_6 based on the measured experimental parameters.

Serial Number	Current (mA)	t_p (s)	Capacity (μAh)	Absorbance at λ_{350nm}
1	0.4	3180	353.4	1.08
2	0.4	3420	380	1.233
3	0.4	3162	352.2	1.08
4	0.4	3426	380.7	1.233
5	0.4	2907	323.2	0.899
6	0.4	2688	298.6	0.769
7	0.8	1064	236.5	0.422
8	0.8	1213	269.8	0.626
9	0.8	1704	378.6	1.29
10	0.8	1563	347.4	1.083
11	0.8	1041	231.5	0.395

Supplementary Table 2. Lithium-ion diffusion coefficients (D_{Li+}) of LSBs assembled with $Ti_3C_2T_x$@PP and PP.

	D_{Li+} (10^{-8} cm^2 S^{-2})		
	Peak A	Peak B	Peak C
PP	2.24	2.45	5.49
$Ti_3C_2T_x$ @PP	5.15	5.09	11.4

Supplementary Table 3. The mass for each component in the lithium–sulfur pouch batteries.

Component	Mass (g)
Cathode	9.92
Anode	4.57
Al foil	1.7
Separator	1.44
Electrolyte	12.0
Tab & package	2.37
Total	32.0

The following equation was used to calculate the specific energy density of the pouch cell:

$$\mathrm{E_g} = \frac{VC}{\sum m_i}$$

where E_g is the energy density (Wh kg^{-1}), V is the average output voltage (V), which is approximately 2.139 V for this pouch cell, C is the discharge capacity (Ah), and m_i is the mass for each component in the pouch cell (g).

References and notes

45. Bai, S., Liu, X., Zhu, K., Wu, S. & Zhou, H. Metal-organic framework-based separator for lithium–sulfur batteries. *Nat. Energy* **1**, 16094 (2016).

46. Guo, W. et al., Artificial dual solid-electrolyte interfaces based on in situ organothiol transformation in lithium sulfur battery. *Nat. Commun.* **12**, 3031 (2021).

47. Yang, Q. et al., Chlorine bridge bond-enabled binuclear copper complex for electrocatalyzing lithium–sulfur reactions. *Nat. Commun.* **15**, 3231 (2024).

48. Kim, H., Lee, J., Ahn, H., Kim, O. & Park, M. J. Synthesis of three-dimensionally interconnected sulfur-rich polymers for cathode materials of high-rate lithium–sulfur batteries. *Nat. Commun.* **6**, 7278 (2015).

49. Pei, F. et al., Interfacial self-healing polymer electrolytes for long-cycle solid-state lithium–sulfur batteries. *Nat. Commun.* **15**, 351 (2024).

50. Huang, Y. et al., Laser induced molybdenum sulphide loading on doped graphene cathode for highly stable lithium sulphur battery. *Commun. Chem.* **2**, 138 (2019).

51. Li, Z. et al., A sulfur host based on titanium monoxide@carbon hollow spheres for advanced lithium–sulfur batteries. *Nat. Commun.* **7**, 13065 (2016).

52. Liu, T. et al., A Li_2S-based all-solid-state battery with high energy and superior safety. *Sci. Adv.* **8**, eabl8390 (2022).

53. Fan, Q., Liu, W., Weng, Z., Sun, Y. & Wang, H. Ternary hybrid material for high-performance lithium–sulfur battery. *J. Am. Chem. Soc.* **137**, 12946–12953 (2015).

54. Duan, H. et al., Scalable synthesis of ultrathin polyimide covalent organic framework nanosheets for high-performance lithium–sulfur batteries. *J. Am. Chem. Soc.* **143**, 19446–19453 (2021).

55. Wang, P. et al., High-performance lithium–sulfur batteries via molecular complexation. *J. Am. Chem. Soc.* **145**, 18865–18876 (2023).

56. Du, Z. et al., Cobalt in nitrogen-doped graphene as single-atom catalyst for high-sulfur content lithium–sulfur batteries. *J. Am. Chem. Soc.* **141**, 3977–3985 (2019).

57. Li, B. et al., Origin of phase engineering $CoTe_2$ alloy toward kinetics-reinforced and dendrite-free lithium–sulfur batteries. *Adv. Mater.* **36**, e2309324 (2024).

58. Wang, P. et al., WSe_2 flakelets on n-doped graphene for accelerating polysulfide redox and regulating li plating. *Angew. Chem. Int. Ed.* **61**, e202116048 (2022).

59. Wang, Y. et al., Binary sulfiphilic nickel boride on boron-doped graphene with beneficial interfacial charge for accelerated lithium–sulfur dynamics. *Small* **19**, e2208281 (2023).

60. Deng, D. R. et al., Accelerating the rate-determining steps of sulfur conversion reaction for lithium–sulfur batteries working at an ultrawide temperature range. *Adv. Mater.* **36**, e2406135 (2024).

61. Yuan, H. et al., Formation of 2D amorphous lithium sulfide enabled by Mo_2C clusters loaded carbon scaffold for high-performance lithium sulfur batteries. *Adv. Mater.* **36**, e2400639 (2024).

62. Geng, C. et al., Superhigh coulombic efficiency lithium–sulfur batteries enabled by in situ coating lithium sulfide with polymerizable electrolyte additive. *Adv. Energy Mater.* **13**, 2204246 (2023).